

Cosmological Constraints from a Combination of Galaxy Clustering and Lensing – III. Application to SDSS Data

Marcello Cacciato^{1*}, Frank C. van den Bosch², Surhud More³, Houjun Mo⁴, Xiaohu Yang⁵

¹*Racah Institute of Physics, The Hebrew University, Jerusalem 91904, Israel*

²*Department of Astronomy, Yale University, P.O. Box 208101, New Haven, CT 06520-8101*

³*Kavli Institute for Cosmological Physics, University of Chicago, 933 East 56th Street, Chicago, IL 60637, USA*

⁴*Department of Astronomy, University of Massachusetts, Amherst MA 01003-9305*

⁵*Key Laboratory for Research in Galaxies and Cosmology, Shanghai Astronomical Observatory, the Partner Group of MPA, Nandan Road 80, Shanghai 200030, China*

ABSTRACT

We simultaneously constrain cosmology and galaxy bias using measurements of galaxy abundances, galaxy clustering and galaxy-galaxy lensing taken from the Sloan Digital Sky Survey. We use the conditional luminosity function (which describes the halo occupation statistics as function of galaxy luminosity) combined with the halo model (which describes the non-linear matter field in terms of its halo building blocks) to describe the galaxy-dark matter connection. We explicitly account for residual redshift space distortions in the projected galaxy-galaxy correlation functions, and marginalize over uncertainties in the scale dependence of the halo bias and the detailed structure of dark matter haloes. Under the assumption of a spatially flat, vanilla Λ CDM cosmology, we focus on constraining the matter density, Ω_m , and the normalization of the matter power spectrum, σ_8 , and we adopt WMAP7 priors for the spectral index, n_s , the Hubble parameter, h , and the baryon density, Ω_b . We obtain that $\Omega_m = 0.278^{+0.023}_{-0.026}$ and $\sigma_8 = 0.763^{+0.064}_{-0.049}$ (95% CL). These results are robust to uncertainties in the radial number density distribution of satellite galaxies, while allowing for non-Poisson satellite occupation distributions results in a slightly lower value for σ_8 ($0.744^{+0.056}_{-0.047}$). These constraints are in excellent agreement (at the 1σ level) with the cosmic microwave background constraints from WMAP. This demonstrates that the use of a realistic and accurate model for galaxy bias, down to the smallest non-linear scales currently observed in galaxy surveys, leads to results perfectly consistent with the vanilla Λ CDM cosmology.

Key words: galaxies: halos — large-scale structure of Universe — dark matter — cosmological parameters — gravitational lensing — methods: statistical

1 INTRODUCTION

The last two decades have seen the emergence of a concordance cosmological model which describes the formation and evolution of cosmic structure in a scenario known as Λ CDM. In these cosmological models, gravity is described by General Relativity, dark matter and dark energy are the major constituents of the Universe (with normal ‘baryonic’ matter only contributing ~ 4 percent), and density perturbations are seeded by quantum fluctuations in a scalar field, the inflaton, that dominated the energy density shortly after

the Big Bang. In its most basic (‘vanilla’) form, the Λ CDM model assumes a flat geometry, dark energy is modeled as Einstein’s cosmological constant, neutrino mass is assumed to be negligible, and the initial power spectrum of density perturbations is assumed to be a single power-law. Such Λ CDM cosmologies are described by 5 parameters: the energy densities (in terms of the critical density) of baryons, Ω_b , and cold dark matter, Ω_{dm} , the spectral index, n_s , and normalization, σ_8 , of the initial power spectrum, and the Hubble parameter, $h = H_0/(100 \text{ km s}^{-1} \text{ Mpc}^{-1})$. The flat geometry implies that $\Omega_\Lambda = 1 - \Omega_m = 1 - \Omega_b - \Omega_{\text{dm}}$, and is strongly supported by the location of the first peak in the angular power spectrum of cosmic microwave background

* E-mail: cacciato@phys.huji.ac.il

(CMB) temperature fluctuations (e.g., Balbi et al. 2000; Lange et al. 2001; Pryke et al. 2002; Netterfield et al. 2002; Ruhl et al. 2003) combined with the results on the Hubble constant from the Hubble Key Project (Freedman et al. 2001).

All these cosmological parameters have now been constrained at the few (~ 3 -20) percent level by a variety of probes, including, among others, temperature anisotropies in the CMB (e.g., Spergel et al. 2003, 2007; Reichardt et al. 2009; Dunkley et al. 2009; Komatsu et al. 2009, 2011), Cepheid distances (e.g., Freedman et al. 2001; Sandage et al. 2006; van Leeuwen et al. 2007), high redshift supernovae Ia (e.g., Riess et al. 1998; Perlmutter et al. 1999, Astier et al. 2006; Kowalski et al. 2008), measurements of the primordial deuterium abundance (e.g., Burles, Nollett & Turner 2001; O’Meara et al. 2006), cluster abundances (e.g., Vikhlinin et al. 2009; Rozo et al. 2010; Benson et al. 2011), cosmic shear (e.g., Benjamin et al. 2007; Fu et al. 2008; Lin et al. 2011), the integrated Sachs-Wolfe effect (e.g., Ho et al. 2008; Giannantonio et al. 2008), the Ly α forest (e.g., Viel, Weller & Haehnelt 2004; McDonald et al. 2005; Desjacques & Nusser 2005), and strong gravitational lensing (e.g., Koopmans et al. 2003; Oguri et al. 2008). Despite some tension between a few subsets of all these independent constraints (see e.g., Dunkley et al. 2009 for a comprehensive overview), overall they are in good mutual agreement, giving rise to the notion of a true concordance cosmology.

Another potentially powerful probe for cosmology is the (large-scale) distribution of galaxies. Although stars make a negligible contribution to the total energy density of the Universe, the light from stars in galaxies can be observed directly and over cosmological scales, making galaxies useful tracers of the underlying dark matter density field. Unfortunately, the connection between galaxies and (dark) matter is muddled by the fact that galaxies are *biased* tracers of the mass distribution. The main problem is that this ‘galaxy bias’ is known to be extremely complicated: it is stochastic (e.g., Dekel & Lahav 1999; Tegmark & Bromley 1999), depends on galaxy properties such as luminosity, color and/or morphological type (e.g., Park et al. 1994; Guzzo et al. 2000; Norberg et al. 2001, 2002; Zehavi et al. 2005, 2011; Wang et al. 2007), and is scale dependent on small scales (e.g., Pervival et al. 2007; Reid, Spergel & Bode 2009; Cacciato et al. 2012). Based on these considerations, it is not surprising that galaxy bias is generally considered a nuisance when using galaxies to constrain cosmology. However, galaxy bias also contains a wealth of information regarding galaxy formation, especially on small scales (e.g., Cacciato et al. 2012). After all, it is the (poorly understood) physics of galaxy formation that determines where, how and with what efficiency galaxies form within the dark matter density field (see Mo, van den Bosch & White 2010). Therefore, ideally, one would like to *simultaneously* solve for cosmology and galaxy bias.

Early attempts to do so used galaxy power spectra measured from the two-Degree Field Galaxy Redshift Survey (2dFGRS; Colless et al. 2003) and/or Sloan Digital Sky Survey (SDSS; York et al. 2000) combined with a phenomenological fitting function for the non-linear, scale-dependent bias and marginalized over its free parameters (e.g., Cole et al. 2005; Tegmark et al. 2006; Padmanabhan et al. 2007). However, this approach has two problems. First, the fitting function used to describe the galaxy bias has no logical con-

nection to galaxy formation. For this reason the free parameters used to parameterize the galaxy bias are merely considered as nuisance parameters. Second, as pointed out by Sánchez & Cole (2008) and Yoo et al. (2009), the particular fitting function used is often a poor description of the true scale dependence of galaxy bias, causing biased estimates of the cosmological parameters, especially for non-vanilla Λ CDM cosmologies (e.g., Hamann et al. 2008). It is generally believed that the latter problem explains why there is still some tension between cosmological parameters (mainly Ω_m) inferred from different galaxy power spectra, or from using the same power spectrum, but using data covering different scales (e.g., Percival et al. 2007; Sánchez & Cole 2008; Dunkley et al. 2009)

This indicates that it is prudent to use a realistic, physically motivated model for galaxy bias. Under the assumption that all galaxies reside in dark matter haloes, a natural, realistic model for galaxy bias is provided by halo occupation models, which describe, in a statistical sense, how galaxies are distributed over dark matter haloes (e.g., Jing, Mo & Börner 1998; Peacock & Smith 2000; Scoccimarro et al. 2001; Berlind & Weinberg 2002; Yang, Mo & van den Bosch 2003). When combined with the halo model, which describes the (non-linear) matter distribution in terms of the dark matter halo building blocks (e.g., Neyman & Scott 1952; Seljak 2000; Ma & Fry 2000; Cooray & Sheth 2002), these halo occupation models provide a complete, accurate, and easy-to-interpret description of galaxy bias, all the way from the large, linear scales down to the small, non-linear scales of individual dark matter haloes.

The problem with this approach, though, is that the halo occupation models are also cosmology dependent, so that one typically needs constraints in addition to just large scale clustering. Several attempts have been made along these lines. Abazajian et al. (2005) simply used strong priors from the WMAP results. Yang et al. (2004) and Tinker et al. (2007) used peculiar velocities as inferred from the redshift space distortions in the two-point correlation function, and argued for a relatively low value of $\sigma_8 \sim 0.7 - 0.75$ (for a vanilla Λ CDM cosmology with $\Omega_m = 0.3$). Similar conclusions were reached by van den Bosch et al. (2003b) and Tinker et al. (2005), who used constraints on the (average) mass-to-light ratios of clusters, rather than peculiar velocities. Somewhat puzzling, a more recent analysis by Tinker et al. (2012) used the mass-to-number ratio of clusters, rather than the mass-to-light ratios, and found a relatively *high* value for σ_8 of 0.85 ± 0.05 (again for $\Omega_m = 0.3$).

In this paper we use a combination of galaxy clustering and galaxy-galaxy lensing, as well as constraints on galaxy abundances, in order to simultaneously constrain cosmology and galaxy bias. Since galaxy-galaxy lensing probes the mass associated with the lensing galaxies, this is similar to using mass-to-light ratios as constraints. It has the advantage, though, that it probes mass-to-light ratios over a wide range in halo masses, and that the same halo occupation model used to compute the clustering of galaxies can also be used to compute the galaxy-galaxy lensing signal (e.g., Guzik & Seljak 2002; Yoo et al. 2006; Cacciato et al. 2009). A first application of this idea by Seljak et al. (2005), when combined with WMAP constraints, yielded a relative high value for σ_8 of 0.88 ± 0.06 (for $\Omega_m \simeq 0.25$). More recently, two different analyses based on the same galaxy-galaxy lensing data

by Cacciato et al. (2009) and Li et al. (2009) both argued that a flat Λ CDM cosmology with $(\Omega_m, \sigma_8) = (0.238, 0.734)$ is in much better agreement with the data than a $(0.3, 0.9)$ model, thus favoring again a relatively low value for σ_8 . In this paper we improve on all these previous methods by (i) simultaneously constraining galaxy bias and cosmology, (ii) using a much more accurate analytical model, (iii) using the latest clustering data, (iv) modelling the latter accounting for residual redshift space distortions, (v) marginalizing over uncertainties related to the detailed structure of dark matter haloes and the scale dependence of the halo bias, and (vi) subjecting the analysis to a number of detailed tests that address how the results depend on certain assumptions inherent to the model.

This paper is the third in a series. In van den Bosch et al. (2012; hereafter Paper I), we presented the analytical model, which we calibrated and tested using detailed mock catalogs constructed from high resolution N -body simulations. We demonstrated that our analytical model is accurate at the level of 10% or better over the entire range of scales covered by the data. In More et al. (2012b; hereafter Paper II), we presented a Fisher matrix analysis to identify parameter-degeneracies and to assess the accuracy with which various cosmological parameters can be constrained using our methodology. We demonstrated that the method can simultaneously constrain halo occupation statistics and cosmology, and we forecasted that, using existing data from the SDSS, we should be able to put constraints on Ω_m and σ_8 that are among the tightest ever achieved. In this paper we apply our method to existing data from the SDSS[†]. Although, as demonstrated in paper II, our method is also able to constrain extensions to the vanilla Λ CDM cosmology, such as neutrino mass and the equation of state of dark energy, in this paper we focus solely on vanilla Λ CDM cosmologies, and in particular on constraining the combination (Ω_m, σ_8) . We defer constraining neutrino mass, dark energy, and other modifications to the vanilla Λ CDM cosmology to future papers.

This paper is organized as follows. In §2, we introduce the SDSS data used to constrain our models. In §3, we briefly review our analytical model to compute the galaxy luminosity function, the galaxy-galaxy correlation function, and the galaxy-galaxy lensing signal using the halo model combined with a model that describes halo occupation statistics as function of galaxy luminosity. The Bayesian analysis, used to infer posterior distributions for the cosmological parameters and for the parameters that describe the halo occupation statistics, is described in §4. Our main results are presented in §5, while §6 describes a number of tests that address the sensitivity of our results to several model assumptions. We summarize our findings in §7.

Throughout this paper, unless specifically stated otherwise, all radii and densities are in comoving units, and log is used to refer to the 10-based logarithm. Quantities that depend on the Hubble parameter are written in units of h , defined above.

[†] A preliminary version of the main results presented in this paper were published in a conference proceedings by More et al. (2012a).

2 DATA

The data used to constrain our models consists of three components: galaxy abundances, in the form of the galaxy luminosity function, galaxy clustering, in the form of projected correlation functions for six different luminosity bins, and galaxy-galaxy lensing, in the form of excess surface densities (ESD), once again for six different luminosity bins. All these measurements are obtained from the Sloan Digital Sky Survey (SDSS; York et al. 2000).

We use the r -band galaxy luminosity function, $\Phi(L)$, (hereafter LF) of Blanton et al. (2003a)[‡], sampled at 32 magnitudes in the range $-23.0 \leq {}^{0.1}M_r - 5 \log h \leq -18.0$, where ${}^{0.1}M_r$ indicates the r -band magnitude of galaxies K+E corrected to $z = 0.1$ following the procedure of Blanton et al. (2003b). For each of these magnitude bins we use the (statistical) errors on Φ quoted by Blanton et al. (2003a). Unfortunately, we do not have a full covariance matrix for this data set. There are two main sources of covariance for the luminosity function: magnitude errors, which cause covariance between neighboring magnitude bins, and large scale structure ('sample variance')[§]. The LF of Blanton et al. is sampled at magnitude intervals of $\delta m_r = 0.00986$ mag, which is much smaller than the typical error on individual magnitudes (~ 0.05 mag). In order to suppress the covariance due to these magnitude errors, we only sample the LF of Blanton et al. at 32 magnitude intervals of $\delta m_r = 0.1578$, roughly three times as large as the typical magnitude error. This should eliminate virtually all covariance due to errors in the magnitudes of individual galaxies. This leaves the covariance due to sample variance, which can be 'modeled' to reasonable accuracy as an up or down shift of the entire LF (i.e., the error bars are fully covariant, e.g. Blanton et al. 2003a). Throughout this study, we ignore this sample variance, which effectively implies that we assume that the volume probed by the SDSS is a fair representation of the average Universe (see discussion in §6.4).

The galaxy clustering data used in this paper are taken from Zehavi et al. (2011), and based on the SDSS DR7 (Abazajian et al. 2009). Using all galaxies in the main galaxy sample with apparent magnitudes $14.5 < m_r < 17.6$, Zehavi et al. measured the projected correlation functions, $w_p(r_p)$, over the radial range $0.2h^{-1} \text{ Mpc} < r_p < 20h^{-1} \text{ Mpc}$ for six volume limited samples (see Table 1). These have been obtained according to

$$w_p(r_p) = 2 \int_0^{r_{\max}} \xi_{\text{gg}}(r_p, r_\pi) dr_\pi. \quad (1)$$

with $r_{\max} = 40h^{-1} \text{ Mpc}$ or $60h^{-1} \text{ Mpc}$, depending on the luminosity sample used (see Table 1). Here r_p is the projected separation between two galaxies, r_π is the redshift-space separation along the line-of-sight, and $\xi_{\text{gg}}(r_p, r_\pi)$ is the two-dimensional correlation function, which is anisotropic due to the presence of peculiar velocities. As discussed in Paper I, the fact that r_{\max} is finite results in residual redshift space distortions that need to be corrected for in the modeling (see also § 6.3). The errors on $w_p(r_p)$ are characterized by

[‡] available at <http://cosmo.nyu.edu/mb144/lf.html>

[§] Following Scott, Srednicki & White (1994) we use the term 'sample variance', rather than the more common 'cosmic variance'

Table 1. Properties of the projected correlation function data

$^{0.1}M_r - 5 \log h$ (1)	z_{\min} (2)	z_{\max} (3)	$\langle z \rangle$ (4)	N_{gal} (5)	r_{\max} (6)
(-18, -17]	0.011	0.026	0.021	5,965	40
(-19, -18]	0.017	0.042	0.032	18,200	40
(-20, -19]	0.027	0.064	0.050	44,348	60
(-21, -20]	0.042	0.106	0.082	108,629	60
(-22, -21]	0.066	0.159	0.123	73,746	60
(-23, -22]	0.103	0.245	0.187	10,251	60

The volume-limited galaxy samples used by Zehavi et al. (2011) to measure the projected correlation function, $w_p(r_p)$. For each of these samples column (1) lists the magnitude range in $^{0.1}M_r - 5 \log h$, columns (2), (3) and (4) list the minimum, maximum and mean redshifts, respectively, column (5) lists the number of galaxies, and column (6) lists the value of r_{\max} (in h^{-1} Mpc), defined in Eq. (1).

their full covariance matrices, kindly provided to us in electronic format by I. Zehavi, and obtained from 144 spatially contiguous subsamples using the jackknife technique.

Finally, for the galaxy-galaxy lensing data we use the excess surface densities, $\Delta\Sigma(R)$, covering the radial range $0.04h^{-1}$ Mpc $< R < 2h^{-1}$ Mpc, obtained by Seljak et al. (2005) and Mandelbaum et al. (2006), and kindly provided to us in electronic format by R. Mandelbaum. These measurements have been obtained using a catalogue of 351, 507 lens galaxies with apparent magnitude $m_r < 17.77$ in the redshift range $0.02 < z < 0.35$ taken from the main galaxy catalogue of the SDSS Data Release 4 (Adelman-McCarthy et al. 2006). This sample is split in 8 (flux-limited) luminosity bins. However, since both the faintest and brightest bins have extremely poor signal-to-noise, we only use the 6 intermediate luminosity bins listed in Table 2. We refer the reader to Mandelbaum et al. (2006) for a detailed description of the data and of the method used to determine the excess surface density profiles. Since the covariance in $\Delta\Sigma(R)$ is only very small over the radial scales covered by the data (R. Mandelbaum, private communication), we only use the diagonal elements in what follows. Throughout this paper we refer to these three data sets as the LF, WP and ESD data. Note that each of these data sets adopted a flat Λ CDM cosmology with $\Omega_m = 0.3$ (LF and WP) or $\Omega_m = 0.27$ (ESD) when computing distances and/or absolute magnitudes. Changing the assumed cosmology, as we do in our analysis, in principle therefore also has a small impact on the observational measurements by changing the distance-redshift relation and thus shifting galaxies among luminosity bins and galaxy pairs among radial separation bins. However, in this paper we restrict ourselves to cosmologies that only differ mildly from a Λ CDM cosmology with $\Omega_m = 0.3$. Even at our outer redshift limit of $z = 0.2$, the effect of lowering Ω_m from 0.3 to 0.25 is only 1 percent in distance, so the measurements used here are effectively independent of cosmological parameters within their observational uncertainties. Therefore, we ignore this small effect in what follows, and always use the observational data as described above.

Table 2. Properties of the excess surface density data

$^{0.1}M_r - 5 \log h$ (1)	$\langle z \rangle$ (2)	N_{lens} (3)
(-19.0, -18.0]	0.047	29,730
(-20.0, -19.0]	0.071	85,766
(-21.0, -20.0]	0.10	141,976
(-21.5, -21.0]	0.14	60,994
(-22.0, -21.5]	0.17	34,920
(-22.5, -22.0]	0.20	13,067

The flux-limited galaxy samples used by Mandelbaum et al. (2006) to measure the excess surface density profiles, $\Delta\Sigma(R)$. For each of these samples column (1) lists the magnitude range in $^{0.1}M_r - 5 \log h$, column (2) lists the mean redshift, and column (3) lists the number of lens galaxies used.

3 MODEL DESCRIPTION

As described in detail in Paper I, the observables[¶] $\Phi(L, z)$, $w_p(r_p, z)$ and $\Delta\Sigma(R, z)$ can be computed for a given cosmology, which determines the properties of the dark matter distribution (e.g. halo mass function, halo bias function, halo density profiles), and a given description of the galaxy-dark matter connection (i.e., halo occupation statistics). The dependence on redshift is included to emphasize that we model each observable at its mean redshift. For the luminosity function we adopt $z = 0.1$, while the mean redshifts for the different luminosity bins of the $w_p(r_p)$ and $\Delta\Sigma(R)$ measurements are listed in Tables 1 and 2, respectively.

In this section we give a concise overview of our model. Readers interested in a more thorough description are referred to Paper I, while those readers that are already familiar with our model, or that are mainly interested in the results, may want to skip this section and proceed immediately to § 4.

3.1 Cosmological Parameters

Throughout this paper we consider ‘vanilla’ Λ CDM cosmologies in which gravity is described by standard General Relativity, neutrino mass is negligible, the initial power spectrum is a single power-law, and dark energy is modeled as Einstein’s cosmological constant with $\Omega_\Lambda = 1 - \Omega_m$. These cosmologies are completely specified by five parameters; the $z = 0$ matter density in units of the critical density, Ω_m , the normalization of the matter power spectrum, σ_8 , the Hubble parameter $h = H_0/(100 \text{ km s}^{-1} \text{ Mpc}^{-1})$, the initial spectral index of the matter power spectrum, n_s , and the $z = 0$ baryon density in units of the critical density, Ω_b . Hence, our cosmological model parameters are described by the vector

$$\lambda^{\text{cosmo}} \equiv (\Omega_m, \sigma_8, h, n_s, \Omega_b h^2). \quad (2)$$

Note that the baryon density only enters in our analysis in the transfer function, and always in the combination $\Omega_b h^2$.

[¶] The projected correlation function and the excess surface density are modeled per luminosity bin $[L_1, L_2]$. However, to keep the notation concise, we do not explicitly write down the dependence on L_1 and L_2 .

The main goal of this paper is to use the observational data on $\Phi(L)$, $w_p(r_p)$ and $\Delta\Sigma(R)$ discussed in §2 to constrain Ω_m and σ_8 . Throughout this paper we will therefore not use any priors on these two parameters. For h , n_s and Ω_b , on the other hand, we include prior information from the seven year analysis of the cosmic microwave background data from WMAP (hereafter WMAP7; Komatsu et al. 2011), as described in §4 below. For this reason we refer to h , n_s and Ω_b as our secondary cosmological parameters in what follows.

3.2 The Conditional Luminosity Function

Under the assumption that each galaxy resides in a dark matter halo, $\Phi(L, z)$, $w_p(r_p, z)$ and $\Delta\Sigma(R, z)$ can be computed using a statistical description of how galaxies are distributed over dark matter haloes of different mass. To that extent we use the conditional luminosity function (hereafter CLF) introduced by Yang et al. (2003). The CLF, $\Phi(L|M)dL$, specifies the *average* number of galaxies with luminosities in the range $L \pm dL/2$ that reside in a halo of mass M . We split the CLF in two components,

$$\Phi(L|M) = \Phi_c(L|M) + \Phi_s(L|M), \quad (3)$$

where $\Phi_c(L|M)$ describes the contribution due to central galaxies (defined as those galaxies that reside at the center of their host halo), while $\Phi_s(L|M)$ characterizes satellite galaxies (those that orbit around a central). Throughout we ignore a potential redshift dependence of the CLF. Since the data that we use to constrain the CLF only covers a narrow range in redshift, this assumption will not have a strong impact on our results.

Our parameterization of the CLF model is motivated by the results obtained by Yang, Mo & van den Bosch (2008) from a large galaxy group catalogue (Yang et al. 2007) extracted from the SDSS Data Release 4, and by Tal et al. (2012) from a study of the luminosity function of satellite galaxies of luminous red galaxies. In particular, the CLF of central galaxies is modeled as a log-normal function:

$$\Phi_c(L|M) dL = \frac{\log e}{\sqrt{2\pi} \sigma_c} \exp \left[-\frac{(\log L - \log L_c)^2}{2\sigma_c^2} \right] \frac{dL}{L}, \quad (4)$$

and the satellite term as a modified Schechter function:

$$\Phi_s(L|M) dL = \phi_s^* \left(\frac{L}{L_s^*} \right)^{\alpha_s + 1} \exp \left[-\left(\frac{L}{L_s^*} \right)^2 \right] \frac{dL}{L}, \quad (5)$$

which decreases faster than a Schechter function at the bright end. Note that L_c , σ_c , ϕ_s^* , α_s and L_s^* are all functions of the halo mass M .

Following Cacciato et al. (2009), and motivated by the results of Yang et al. (2008) and More et al. (2009, 2011), we assume that σ_c , which expresses the scatter in $\log L$ of central galaxies at fixed halo mass, is a constant (i.e. is independent of halo mass and redshift). In addition, for L_c , we adopt the following parameterization;

$$L_c(M) = L_0 \frac{(M/M_1)^{\gamma_1}}{[1 + (M/M_1)^{\gamma_1 - \gamma_2}]}. \quad (6)$$

Hence, $L_c \propto M^{\gamma_1}$ for $M \ll M_1$ and $L_c \propto M^{\gamma_2}$ for $M \gg M_1$. Here M_1 is a characteristic mass scale, and $L_0 = 2^{\gamma_1 - \gamma_2} L_c(M_1)$ is a normalization.

For the satellite galaxies we adopt

$$L_s^*(M) = 0.562 L_c(M), \quad (7)$$

$$\alpha_s(M) = \alpha_s \quad (8)$$

(i.e., the faint-end slope of $\Phi_s(L|M)$ is independent of mass and redshift), and

$$\log[\phi_s^*(M)] = b_0 + b_1(\log M_{12}) + b_2(\log M_{12})^2, \quad (9)$$

with $M_{12} = M/(10^{12} h^{-1} M_\odot)$. Note that neither of these functional forms has a physical motivation; they merely were found to adequately describe the results obtained by Yang et al. (2008) from the SDSS galaxy group catalog.

To summarize, our parameterization of the CLF thus has a total of nine free parameters, characterized by the vector

$$\lambda^{\text{CLF}} \equiv (\log M_1, \log L_0, \gamma_1, \gamma_2, \sigma_c, \alpha_s, b_0, b_1, b_2). \quad (10)$$

3.3 Galaxy Luminosity Function

Once the CLF is specified, the galaxy luminosity function at redshift z , $\Phi(L, z)$, simply follows from integrating over the halo mass function, $n(M, z)$;

$$\Phi(L, z) = \int \Phi(L|M) n(M, z) dM. \quad (11)$$

In what follows, we will always be concerned with galaxies in a specific luminosity interval $[L_1, L_2]$. The average number density of such galaxies follows from the CLF according to

$$\bar{n}_g(z) = \int \langle N_g|M \rangle n(M, z) dM, \quad (12)$$

where

$$\langle N_g|M \rangle = \int_{L_1}^{L_2} \Phi(L|M) dL, \quad (13)$$

is the average number of galaxies with $L_1 < L < L_2$ that reside in a halo of mass M .

3.4 Power-Spectra

The first step towards computing the projected correlation functions, $w_p(r_p, z)$, and ESD profiles, $\Delta\Sigma(R, z)$, is to compute the galaxy-galaxy power spectrum, $P_{gg}(k, z)$, and the galaxy-matter cross power spectrum, $P_{gm}(k, z)$. These power spectra are the Fourier space analogs of the galaxy-galaxy and galaxy-matter correlation functions.

The galaxy-galaxy power spectrum can be expressed as a sum of the one-halo (1h) and the two-halo (2h) terms, each of which can be further subdivided based upon the type of galaxies (central or satellite) that contribute to the power spectrum, i.e.,

$$P_{gg}(k) = 2P_{cs}^{1h}(k) + P_{ss}^{1h}(k) + P_{cc}^{2h}(k) + 2P_{cs}^{2h}(k) + P_{ss}^{2h}(k). \quad (14)$$

Similarly, the galaxy-matter power spectrum can be written as

$$P_{gm}(k) = P_{cm}^{1h}(k) + P_{sm}^{1h}(k) + P_{cm}^{2h}(k) + P_{sm}^{2h}(k). \quad (15)$$

As shown in paper I, these terms can be written in compact form as

$$P_{xy}^{1h}(k, z) = \int \mathcal{H}_x(k, M, z) \mathcal{H}_y(k, M, z) n(M, z) dM, \quad (16)$$

$$P_{xy}^{2h}(k, z) = \int dM_1 \mathcal{H}_x(k, M_1, z) n(M_1, z) \int dM_2 \mathcal{H}_y(k, M_2, z) n(M_2, z) Q(k|M_1, M_2, z), \quad (17)$$

where ‘x’ and ‘y’ are either ‘c’ (for central), ‘s’ (for satellite), or ‘m’ (for matter), $Q(k|M_1, M_2, z)$ describes the power-spectrum of haloes of mass M_1 and M_2 (see Appendix A), and we have defined

$$\mathcal{H}_m(k, M, z) = \frac{M}{\bar{\rho}_m} \tilde{u}_h(k|M, z), \quad (18)$$

$$\mathcal{H}_c(k, M, z) = \mathcal{H}_c(M, z) = \frac{\langle N_c|M \rangle}{\bar{n}_g(z)}, \quad (19)$$

and

$$\mathcal{H}_s(k, M, z) = \frac{\langle N_s|M \rangle}{\bar{n}_g(z)} \tilde{u}_s(k|M, z). \quad (20)$$

Here $\langle N_c|M \rangle$ and $\langle N_s|M \rangle$ are the average number of central and satellite galaxies in a halo of mass M , which follow from Eq. (13) upon replacing $\Phi(L|M)$ by $\Phi_c(L|M)$ and $\Phi_s(L|M)$, respectively. Furthermore, $\tilde{u}_s(k|M)$ is the Fourier transform of the normalized number density distribution of satellite galaxies that reside in a halo of mass M , and $\tilde{u}_h(k|M)$ is the Fourier transform of the normalized density distribution of dark matter within a halo of mass M .

3.5 Computing $w_p(r_p, z)$ and $\Delta\Sigma(R, z)$

Once $P_{gg}(k, z)$ and $P_{gm}(k, z)$ have been determined, it is fairly straightforward to compute the projected galaxy-galaxy correlation function, $w_p(r_p, z)$, and the excess surface density (ESD) profile, $\Delta\Sigma(R, z)$. We start by Fourier transforming the power-spectra to obtain the two-point correlation functions:

$$\xi_{gx}(r, z) = \frac{1}{2\pi^2} \int_0^\infty P_{gx}(k, z) \frac{\sin kr}{kr} k^2 dk, \quad (21)$$

where ‘x’ is either ‘g’ (for galaxies) or ‘m’ (for matter).

The projected galaxy-galaxy correlation function, $w_p(R, z)$, is related to the real-space galaxy-galaxy correlation function, $\xi_{gg}(r, z)$, according to

$$\begin{aligned} w_p(r_p, z) &= 2 \int_0^{r_{\max}} \xi_{gg}(r_p, r_\pi, z) dr_\pi \\ &= 2 \sum_{l=0}^2 \int_0^{r_{\max}} \xi_{2l}(s, z) \mathcal{P}_{2l}(r_\pi/s) dr_\pi. \end{aligned} \quad (22)$$

Here r_{\max} is the maximum integration range used for the data (see Table 1), r_π is the separation perpendicular to the line-of-sight, $s = \sqrt{r_p^2 + r_\pi^2}$ is the separation between the galaxies in redshift space, $\mathcal{P}_l(x)$ is the l^{th} Legendre polynomial, and ξ_0 , ξ_2 , and ξ_4 are given by

$$\xi_0(r, z) = \left(1 + \frac{2}{3}\beta + \frac{1}{5}\beta^2\right) \xi_{gg}(r, z), \quad (23)$$

$$\xi_2(r, z) = \left(\frac{4}{3}\beta + \frac{4}{7}\beta^2\right) [\xi_{gg}(r, z) - 3J_3(r, z)], \quad (24)$$

$$\xi_4(r, z) = \frac{8}{35}\beta^2 \left[\xi_{gg}(r, z) + \frac{15}{2}J_3(r, z) - \frac{35}{2}J_5(r, z)\right], \quad (25)$$

where

$$J_n(r, z) = \frac{1}{r^n} \int_0^r \xi_{gg}(y, z) y^{n-1} dy. \quad (26)$$

and

$$\beta = \beta(z) = \frac{1}{b(z)} \left(\frac{d \ln D}{d \ln a}\right)_z \simeq \frac{\Omega_m^{0.6}(z)}{b(z)} \quad (27)$$

with $a = 1/(1+z)$ the scale factor, $D(z)$ the linear growth rate, and

$$\bar{b}(z) = \frac{1}{\bar{n}_g(z)} \int \langle N_g|M \rangle b_h(M, z) n(M, z) dM, \quad (28)$$

the mean bias of the galaxies in consideration. Note that Eq. (22) accounts for the large scale redshift space distortions due to infall (the ‘Kaiser’-effect), which is necessary because the measurements for $w_p(p)$ have been obtained using a finite r_{\max} . Note that the $\xi_{gg}(r)$ in Eqs. (23)-(25) is the non-linear galaxy-galaxy correlation function. Although the Kaiser formalism (Kaiser 1987) is only strictly valid in the linear regime, this simple modification results in a more accurate correction for the residual redshift space distortions (see Paper I for details). As shown in Paper I, not taking these residual redshift space distortions into account results in systematic errors that can easily exceed 20 percent on large scales ($r_p \gtrsim 10h^{-1}$ Mpc), causing systematic errors in the inferred galaxy bias (see also Padmanabhan, White & Eisenstein 2007; Norberg et al. 2009; Baldauf et al. 2010; More 2011).

Finally, the excess surface density profile, $\Delta\Sigma(R, z)$, is defined as

$$\Delta\Sigma(R, z) = \frac{2}{R^2} \int_0^R \Sigma(R', z) R' dR' - \Sigma(R, z) \quad (29)$$

Here $\Sigma(R, z)$ is the projected surface mass density, which is related to the galaxy-dark matter cross correlation, $\xi_{gm}(r, z)$, according to

$$\Sigma(R, z) = 2\bar{\rho}_m \int_R^\infty [1 + \xi_{gm}(r, z)] \frac{r dr}{\sqrt{r^2 - R^2}}. \quad (30)$$

3.6 Model Ingredients

In this subsection we briefly describe the ingredients of our model. A more detailed description can be found in Paper I.

In our fiducial model we require both the linear and the non-linear power spectra of the matter distribution, $P_{mm}^{\text{lin}}(k, z)$ and $P_{mm}(k, z)$, respectively. The latter enters in the computation of the halo-halo correlation function, as described in detail in Appendix A. Throughout we compute $P_{mm}(k, z)$ using the fitting formula of Smith et al. (2003)^{||}, while for $P_{mm}^{\text{lin}}(k, z)$ we use the linear transfer function of Eisenstein & Hu (1998), neglecting any contribution from neutrinos and assuming a CMB temperature of 2.725K (Mather et al. 1999).

^{||} We use the small modification suggested on John Peacock’s website <http://www.roe.ac.uk/~jap/haloes/>, although we have verified that this has no significant impact on any of our results.

Table 3. List of models

Model	ψ	η	\mathcal{R}	\mathcal{P}	RRSD	SGW	χ^2_{LF}	χ^2_{WP}	χ^2_{ESD}	χ^2_{prior}	χ^2_{red}
(1)	(2)	(3)	(4)	(5)	(6)	(7)	(8)	(9)	(10)	(11)	(12)
Fiducial	$\mathcal{G}(0.9, 0.15)$	$\mathcal{G}(0.0, 0.1)$	1.0	1.0	yes	yes	47	236	117	4	2.36
Radial	$\mathcal{G}(0.9, 0.15)$	$\mathcal{G}(0.0, 0.1)$	$\mathcal{G}(1.0, 0.25)$	1.0	yes	yes	40	240	118	5	2.36
Poisson	$\mathcal{G}(0.9, 0.15)$	$\mathcal{G}(0.0, 0.1)$	1.0	$\mathcal{G}(1.0, 0.1)$	yes	yes	52	229	113	7	2.35
noRSSD	$\mathcal{G}(0.9, 0.15)$	$\mathcal{G}(0.0, 0.1)$	1.0	1.0	no	yes	48	218	114	5	2.25
noSGW	$\mathcal{G}(0.9, 0.15)$	$\mathcal{G}(0.0, 0.1)$	1.0	1.0	yes	no	32	155	111	16	1.99

List of models described in the text. Column (1) indicates the model name. Columns (2) to (5) indicate the priors used for the parameters ψ , η , \mathcal{R} and \mathcal{A}_{P} . Here $\mathcal{G}(\bar{x}, \sigma)$ indicates a Gaussian prior centered on \bar{x} and with a standard deviation σ . Column (6) indicates whether or not the model corrected for residual redshift space distortions (RRSD), and Column (7) indicates whether or not the Sloan great wall (SGW) is included in the clustering data. Finally, Columns (8) to (12) list the various χ^2 values of the best-fit models in each MCMC chain. The reduced χ^2 value in Column (12) is computed for $N_{\text{dof}} = 171$ degrees of freedom (see §5).

Throughout, we define dark matter haloes as spheres with an average density of 200 times the background density. We assume that their density profiles follow the NFW profile (Navarro, Frenk & White 1997), with a concentration-mass relation given by

$$c(M, z) = (1 + \eta) \bar{c}(M, z). \quad (31)$$

Here $\bar{c}(M, z)$ is the average concentration-mass relation of Macciò et al. (2007), properly converted to our definition of halo mass. We treat η as a free nuisance parameter which accounts for (i) the fact that there is an uncertainty of ~ 10 percent in the average concentration mass relation as obtained by different authors (e.g., Navarro, Frenk & White 1997; Eke, Navarro & Steinmetz 2001; Bullock et al. 2001; Macciò et al. 2007; Zhao et al. 2009), and (ii) realistic dark matter haloes are triaxial, rather than spherical, have substructure, and have scatter in the concentration-mass relation. As shown in Paper I, setting $\eta = \pm 0.2$ modifies the one-halo term of $\xi_{\text{gm}}(r)$ by more than 20 percent on small scales ($r < 0.1 h^{-1}$ Mpc). As discussed at length in Paper I, an uncertainty in η of this amount is more than adequate to capture the inaccuracies in our model that arise from the various oversimplifications and uncertainties regarding the structure of dark matter haloes. Hence, in what follows, we adopt a Gaussian prior on η , centered on $\eta = 0$ and with a standard deviation $\sigma_{\eta} = 0.1$.

For the halo mass function, $n(M, z)$, and the halo bias function, $b_{\text{h}}(M, z)$, we use the fitting functions of Tinker et al. (2010). Note that these functions obey the normalization condition

$$\frac{1}{\bar{\rho}(z)} \int M n(M, z) b_{\text{h}}(M, z) dM = 1 \quad (32)$$

as required by the fact that, on average, on large scales matter is unbiased with respect to itself. As described in Appendix A, the scale dependence of the halo bias in the quasi-linear regime is described by a modified version of the empirical fitting function of Tinker et al. (2005). This modification is needed to account for the fact that we use a different definition of dark matter haloes, and is characterized by one free ‘nuisance’ parameter, ψ . In Paper I we calibrated ψ using numerical N -body simulations of structure formation in a Λ CDM cosmology, and found that $\psi = 0.9$ can accurately fit the simulation results. In order to account for the fact that we cannot rule out that ψ is cosmology de-

pendent, we include an uncertainty of ~ 15 percent on ψ in our cosmological analysis. In particular, we treat ψ as a free parameter, but adopt a Gaussian prior centered on $\psi = 0.9$ and with $\sigma_{\psi} = 0.15$.

For our fiducial model, we assume that the radial number density distribution of satellite galaxies follows that of the dark matter particles, i.e., $u_{\text{s}}(r|M) = u_{\text{h}}(r|M)$. In other words, we assume that satellite galaxies follow a NFW profile with the same concentration-mass relation (Eq. [31]) as dark matter haloes. In §6.1 we relax this assumption and examine how changes in $u_{\text{s}}(r|M)$ impact on our results.

Finally, we emphasize that the expression for the 1-halo term of the galaxy-galaxy correlation function (Eq. [16]) has made the implicit assumption that the halo occupation number of satellite galaxies obeys Poisson statistics, i.e., that $\langle N_{\text{s}}(N_{\text{s}} - 1)|M \rangle = \langle N_{\text{s}}|M \rangle^2$ (see Paper I for details). In §6.2 we will relax this assumption, and explore how deviations of $P(N_{\text{s}}|M)$ from a Poisson distribution impact on our results.

4 METHODOLOGY

The main goal of this paper is to obtain constraints on the cosmological parameters Ω_{m} and σ_{s} , and the halo occupation distribution, as characterized by the CLF, using the SDSS data described in §2 and the analytical model described in §3. We use Bayesian inference techniques to determine the posterior probability distribution $P(\lambda|\mathcal{D})$ of the model parameters λ , given the data \mathcal{D} . According to Bayes’ theorem,

$$P(\lambda|\mathcal{D}) = \frac{P(\mathcal{D}|\lambda) P(\lambda)}{P(\mathcal{D})}, \quad (33)$$

where $P(\mathcal{D}|\lambda)$ is the *likelihood* of the data given the model parameters, $P(\lambda)$ is the *prior probability* of these parameters, and

$$P(\mathcal{D}) = \int P(\mathcal{D}|\lambda) P(\lambda) d\lambda, \quad (34)$$

is the *marginal probability* of the data, also called evidence for the model. Since, we do not intend to perform model selection, the evidence just acts as a normalization constant which need not be calculated. Therefore the posterior distribution $P(\lambda|\mathcal{D})$ is given by

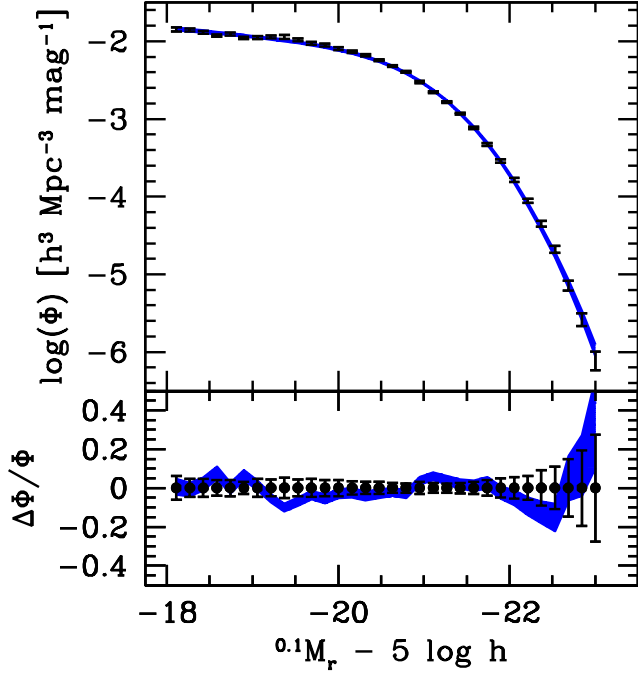


Figure 1. *Upper panel:* The SDSS galaxy luminosity function in the r -band, $K+E$ corrected to $z = 0.1$. Data points with error bars are taken from Blanton et al. (2003a), as described in §2. The shaded region indicates the 95% confidence levels of our **Fiducial** model, as obtained from the corresponding MCMC. *Lower panel:* The corresponding fractional errors, $\Delta\Phi/\Phi$.

$$P(\lambda|\mathcal{D}) \propto \exp\left[\frac{-\chi^2(\lambda)}{2}\right], \quad (35)$$

where $\chi^2(\lambda)$ is a sum of the following terms

$$\chi^2(\lambda) = \chi_{\text{LF}}^2 + \chi_{\text{WP}}^2 + \chi_{\text{ESD}}^2 + \chi_{\text{prior}}^2. \quad (36)$$

The first three terms quantify the goodness of the fit to the data and correspond to the likelihood of the data given the parameters, while the last term corresponds to the prior information we adopt. The likelihood terms are given by

$$\chi_{\text{LF}}^2 = \sum_{j=1}^{32} \left[\frac{\Phi(L_j) - \tilde{\Phi}(L_j)}{\sigma_{\Phi}(L_j)} \right]^2, \quad (37)$$

$$\chi_{\text{WP}}^2 = \sum_{k=1}^6 [\mathbf{w}_p(z_k) - \tilde{\mathbf{w}}_p(z_k)]^T \mathbf{C}_{\text{WP}}^{-1} [\mathbf{w}_p(z_k) - \tilde{\mathbf{w}}_p(z_k)], \quad (38)$$

$$\chi_{\text{ESD}}^2 = \sum_{k=1}^6 \sum_{j=1}^{12} \left[\frac{\Delta\Sigma(R_j, z_k) - \tilde{\Delta\Sigma}(R_j, z_k)}{\sigma_{\Delta\Sigma}(R_j, z_k)} \right]^2. \quad (39)$$

Here \tilde{X} denotes the model prediction for the observable X , σ_X is the corresponding error, $\mathbf{w}_p(z_k)$ is the vector of the projected clustering measurements in the k -th luminosity bin, and \mathbf{C}_{WP} is the covariance matrix of these measurements.

As detailed in Paper I, our analytical model is accurate at the level of 10 (in most cases 5) percent, in reproducing the 3-dimensional galaxy-galaxy correlation and the galaxy-matter cross-correlation from mock galaxy catalogs. Since the differences are not systematic, the accuracy is expected

to be much better for the projected galaxy-galaxy correlation function, $w_p(r_p)$, and the galaxy-galaxy lensing signal, $\Delta\Sigma(R)$. Therefore, we do not account for any systematic uncertainty from our modeling in our likelihood estimate.

For our fiducial model, the set of model parameters, λ , includes our primary cosmological parameters of interest, Ω_m and σ_8 , the set of secondary cosmological parameters ($\Omega_b h^2, n_s, h$), the CLF parameters λ_{CLF} and a set of nuisance parameters (ψ, η). Throughout we adopt uniform, non-informative priors on our primary cosmological parameters as well as on all CLF parameters. For the secondary cosmological parameters, $\lambda_{\text{sec}} = (\Omega_b h^2, n_s, h)$, we include priors from the WMAP7 analysis. In order to obtain the covariance matrix of these parameters (\mathbf{C}_{sec}), we have used the Monte Carlo Markov chains from the WMAP7 analysis (kindly provided to us by E. Komatsu) and marginalized over all other parameters present in their analysis. Finally, for the two nuisance parameters we adopt Gaussian priors, as discussed in §3.6. Hence, we have that

$$\chi_{\text{prior}}^2 = [\lambda_{\text{sec}} - \tilde{\lambda}_{\text{sec}}]^T \mathbf{C}_{\text{sec}}^{-1} [\lambda_{\text{sec}} - \tilde{\lambda}_{\text{sec}}] + \sum_i \left(\frac{\lambda_i - \tilde{\lambda}_i}{\sigma_{\lambda_i}} \right)^2, \quad (40)$$

where the summation is over the two nuisance parameters ψ and η .

We sample the posterior distribution of our model parameters given the data using a Monte-Carlo Markov chain (MCMC). In particular, we implement the Metropolis-Hastings algorithm to construct the MCMC (Metropolis et al. 1953; Hastings 1970). At any point in the chain, a trial model is generated using a method specified below. The chi-squared statistic for the trial model, χ_{try}^2 , is calculated using Equations (36)–(40). This trial model is accepted to be a member of the chain with a probability given by

$$P_{\text{accept}} = \begin{cases} 1.0 & \text{if } \chi_{\text{try}}^2 \leq \chi_{\text{cur}}^2 \\ \exp[-(\chi_{\text{try}}^2 - \chi_{\text{cur}}^2)/2] & \text{if } \chi_{\text{try}}^2 > \chi_{\text{cur}}^2 \end{cases}, \quad (41)$$

where χ_{cur}^2 denotes the χ^2 for the current model in the chain. We initialize the chain from a random position in our multi-dimensional parameter space and obtain a chain of $\sim 50,000$ models. We discard the first 2000 models (the *burn-in* period) allowing the chain to sample from a more probable part of the distribution. We use this chain of models to estimate the confidence levels on the parameters and different observables of interest.

A proper choice of the proposal distribution is very important in order to achieve fast convergence and a reasonable acceptance rate for the trial models. The posterior distribution in a multi-dimensional parameter space, such as the one we are dealing with, will have numerous degeneracies and in general can be very difficult to sample from. We have adopted the following strategy to overcome these difficulties. During the first half of the burn-in stage, we chose an independent Gaussian proposal distribution for every model parameter, as is common for the Metropolis-Hastings algorithm. Half-way through the burn-in stage, we perform a Fisher information matrix analysis at the best fit model found thus far. The Fisher information matrix, given by

$$F_{ij} = -\frac{\partial^2 \ln \mathcal{L}}{\partial \lambda_i \partial \lambda_j}, \quad (42)$$

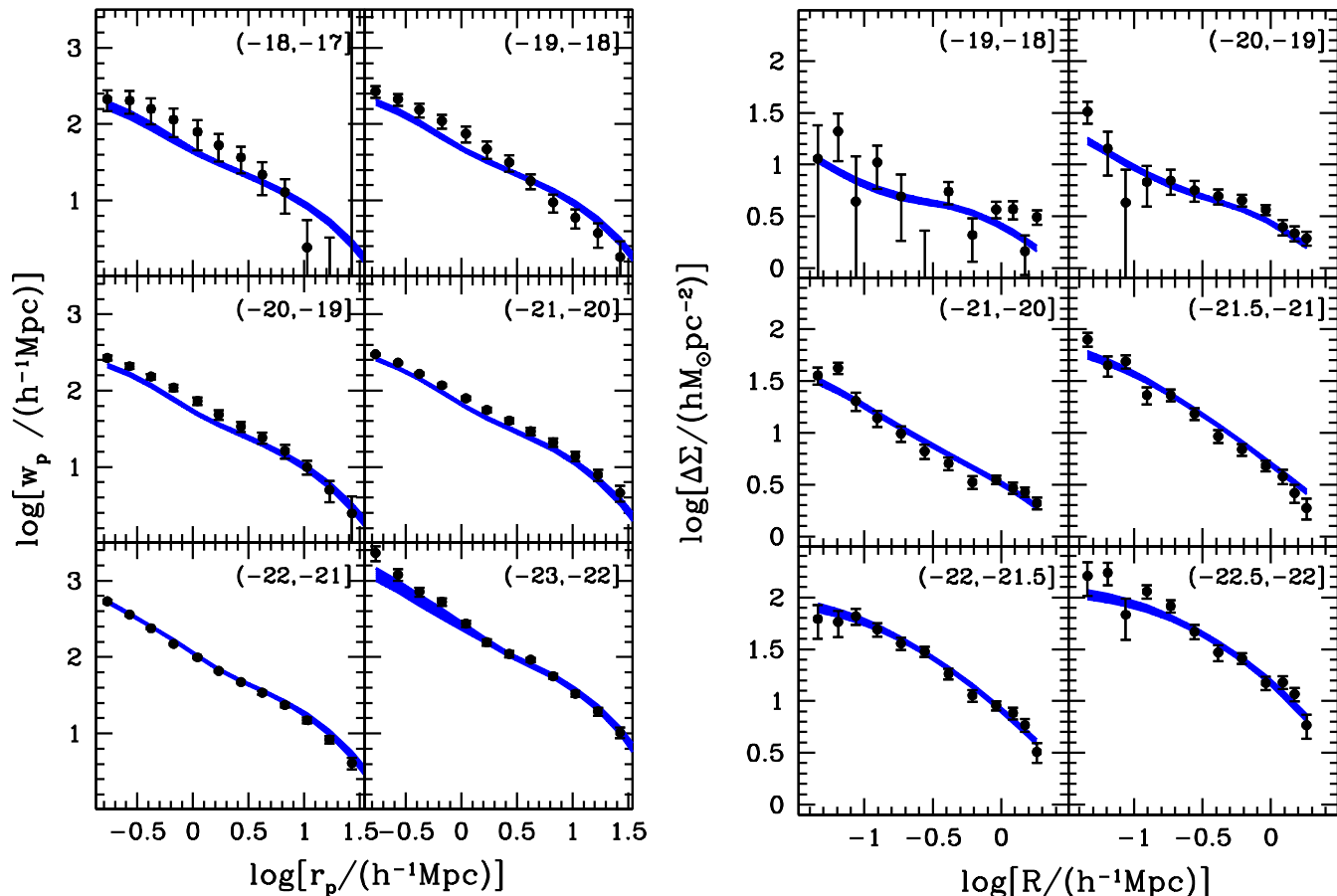


Figure 2. *Left-hand Panel.* Projected correlation functions, $w_p(r_p)$, for the six different magnitude bins listed in Table 1, as indicated. Solid dots with (1σ) error bars are the SDSS data taken from Zehavi et al. (2011), while the shaded regions indicate the 95% confidence levels obtained from the MCMC of our Fiducial model. We caution that, because of the covariance in the data, which is accounted for in the modeling (see §4), the quality of the fit cannot be judged by eye. *Right-hand Panel.* Excess surface density profiles, $\Delta\Sigma(R)$, for the six magnitude bins listed in Table 2, as indicated. Solid dots with (1σ) error bars are the SDSS data of Seljak et al. (2005) and Mandelbaum et al. (2006). As in the left-hand panels, the shaded regions indicate the 95% confidence levels of our Fiducial model.

is a $N_p \times N_p$ symmetric matrix, where N_p denotes the number of parameters in our model, and $\mathcal{L} \propto e^{-\chi^2/2}$ is the likelihood. The inverse of the Fisher matrix gives the covariance matrix, \mathbf{C}_{prop} , of the posterior constraints on the model parameters (see Paper II)^{**}. More importantly, the eigenvectors of the covariance matrix are an excellent guide to the numerous degeneracies in the posterior distribution, and the corresponding eigenvalues set a scale for how wide the posterior ought to be in a given direction. Therefore, for the second half of the burn-in period, we utilize this information and use a proposal distribution which is a multi-variate Gaussian centered at the current value of the parameters and with a covariance equal to \mathbf{C}_{prop} . In practice, the trial model (λ_{try}) can be generated from the current model (λ_{cur}) using

$$\lambda_{\text{try}} = \lambda_{\text{cur}} + \varsigma \mathbf{A} \mathbf{x}, \quad (43)$$

^{**} The subscript ‘prop’ indicates that this matrix is used to describe the proposal distribution.

where \mathbf{x} is a vector consisting of N_p standard normal deviates, the matrix \mathbf{A} is such that $\mathbf{A}\mathbf{A}^T = \mathbf{C}_{\text{prop}}$, and ς is a parameter that we have chosen to achieve an average acceptance rate of $\sim 25\%$. We repeat the Fisher matrix analysis once again at the end of the burn-in period (using the best fit model found thus far) and use the covariance matrix to define our proposal distribution to be used for the MCMC. We have found this strategy to be extremely efficient in sampling our posterior distributions^{††}.

5 RESULTS

Having described the data, the model, and the methodology, we now turn to our results. In this section we describe the cosmological constraints obtained for our Fiducial model, whereas §6 discusses the robustness of these results to model

^{††} A general-purpose python implementation of the MCMC sampler we have used in our work is available from the authors upon request.

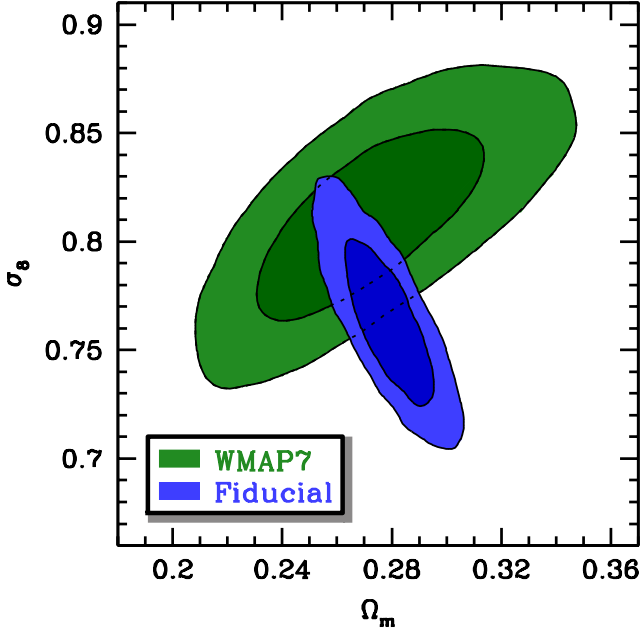


Figure 3. The 68% and 95% CLs of the joint two-dimensional, marginalized posterior distribution for our **Fiducial** model, obtained from the simultaneous analysis of the abundance, clustering and lensing of galaxies in the SDSS. The green contours show the corresponding CLs for the WMAP7 analysis of the CMB (Komatsu et al. 2011), and are shown for comparison.

variations. The constraints on galaxy bias, as characterized via the CLF, are discussed in §5.3.

As discussed above, our **Fiducial** model consists of 16 free parameters; the two primary cosmological parameters of interest, Ω_m and σ_8 , for which we use uniform, non-informative priors, the secondary cosmological parameters n_s , h and $\Omega_b h^2$, for which we use priors from WMAP7 (including their covariance), the 9 CLF parameters that describe the halo occupation statistics, also with uniform, non-informative priors, and finally the 2 nuisance parameters, ψ and η , for which we adopt Gaussian priors as described in §3.6. With a grand total of 182 constraints (32 data points for the LF, six bins of 13 data points each for the projected correlation function^{‡‡} and six bins of 12 ESD data points), this implies $182 - 16 + 5 = 171$ degrees of freedom, which is the number we have used to compute the reduced χ^2 values listed in the final column of Table 3.

Figs. 1 and 2 compare the predictions of the **Fiducial** model (shaded regions, indicating the 95% confidence levels) to the data used to constrain the model (solid dots with error bars, indicating the 68% confidence levels). Fig. 1 shows that the model accurately fits the r -band galaxy luminosity function. Although most data points agree with the model predictions at the 1σ level, the data reveals a few small ‘wiggles’ at the faint end that are not reproduced by the model, and which contribute dominantly to χ^2_{LF} , the value of which is listed in Table 3.

^{‡‡} Although the galaxy-galaxy clustering data points have covariance, we have verified that the covariance matrix for each luminosity bin has rank equal to 13, and therefore does not reduce the number of constraints.

The left-hand side of Fig. 2 shows the projected correlation functions, $w_p(r_p)$, for six different magnitude bins. We caution that, because of the covariance in the data, which is accounted for in the modeling (see §4), the quality of the fit cannot be judged by eye. However, it is evident from the χ^2 values of the best-fit **Fiducial** model (see Table 3), that the total χ^2 is clearly dominated by χ^2_{WP} . In particular, $\chi^2_{\text{WP}} > 2\chi^2_{\text{ESD}}$, even though the projected correlation functions only have $78/72 \simeq 1.08$ times as many data points. It turns out χ^2_{WP} is dominated by the contribution from the data in the $[-20, -21]$ magnitude bin. Interestingly, this bin covers the volume that encloses the Sloan Great Wall (SGW), a huge supercluster at $z \sim 0.08$ and the largest coherent structure detected in the SDSS (Gott et al. 2005). As discussed in Zehavi et al. (2011), pruning the data sample so as to exclude the SGW region results in a significantly reduced clustering strength for galaxies in the $[-20, -21]$ magnitude range (i.e., the correlation length is reduced from $r_0 = 5.46 \pm 0.15$ to 4.82 ± 0.23). We return to this issue, and its potential impact on our cosmological constraints, in §6.4 when we discuss the potential impact of sample variance.

Finally, the right-hand side of Fig. 2 shows the excess surface densities, $\Delta\Sigma(R)$, again for six different magnitude bins as indicated. The model nicely reproduces the overall trends in the data, with only a few data points that fall outside the 95% confidence region of the model. Overall, we conclude that our **Fiducial** model is consistent with the data at a satisfactory level. In particular, the most important features in the data are nicely reproduced by the model and find a natural explanation within the framework of the halo model. For example, the fact that brighter galaxies reveal stronger clustering and higher excess surface densities is consistent with the common notion that brighter galaxies reside in more massive haloes. The lensing signal is directly sensitive to this aspect because it probes the matter distribution around galaxies, whereas the clustering signal is affected by it only indirectly due to the fact that more massive haloes are more strongly clustered than less massive ones (e.g., Mo & White 1996). Also, the relatively weak deviations of $w_p(r_p)$ and $\Delta\Sigma(R)$ from pure power-laws typically reflect transitions from scales where the signal is dominated by different components of the power spectra. Examples are the 1-halo to 2-halo transition (e.g., Zehavi et al. 2004) and the 1-halo central to 1-halo satellite transition for the excess surface densities (e.g., Cacciato et al. 2009).

5.1 Cosmological Parameters

Fig. 3 shows the constraints on our two primary cosmological parameters of interest; Ω_m and σ_8 . The blue contours show the 68% and 95% CLs of the joint two-dimensional, marginalized posterior distribution obtained from our simultaneous analysis of the abundance, clustering and lensing of galaxies in the SDSS. The green contours show the corresponding CLs for the WMAP7 analysis of the CMB (Komatsu et al. 2011), and are shown for comparison. Note that our results are in excellent agreement with those from WMAP7, strengthening the case for a true concordance cosmology. In particular, our analysis yields $\Omega_m = 0.278^{+0.023}_{-0.026}$ and $\sigma_8 = 0.763^{+0.064}_{-0.049}$ (both 95% CL), while the WMAP7 analysis has $\Omega_m = 0.264^{+0.064}_{-0.049}$ and $\sigma_8 = 0.801^{+0.059}_{-0.058}$ (both 95% CL). Note also that the degeneracy between Ω_m and

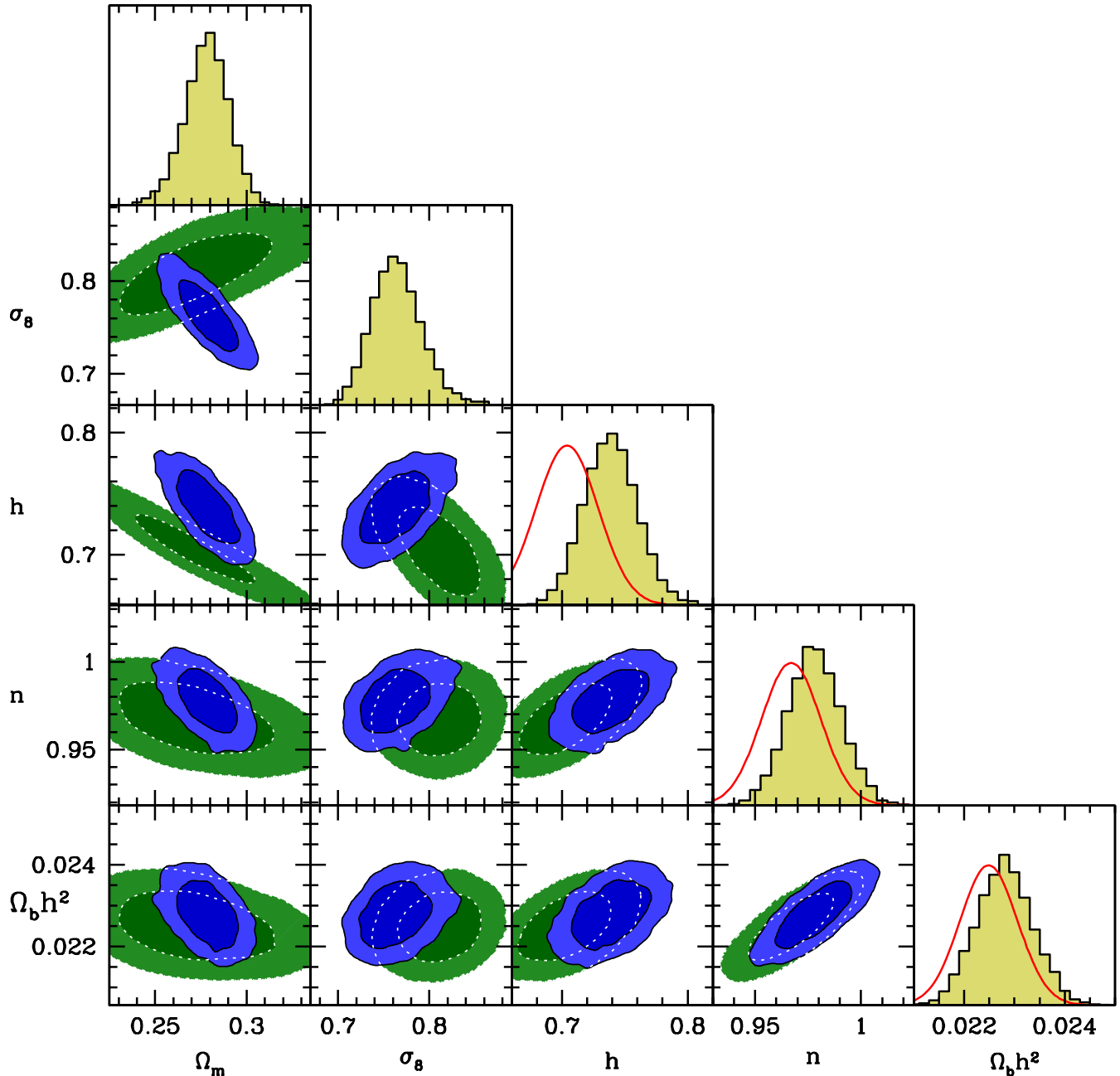


Figure 4. Cosmological constraints for the Fiducial model. Histograms show the marginalized posterior distributions, while the blue contour show the 68% and 95% CLs of the joint, two-dimensional marginalized posterior distributions. For comparison, the corresponding CLs from WMAP7 are shown as green contours, while the red, solid curves show the marginalized WMAP7 prior distributions used for the secondary cosmological parameters, n_s , h and $\Omega_b h^2$.

σ_8 inherent in our analysis runs perpendicular to that inherent in the CMB data. This indicates that a combined analysis will be able to significantly tighten the constraints on Ω_m and σ_8 (see also Paper II). Finally, Fig. 3 suggests that our constraints are even tighter than those from the WMAP7 analysis. However, we emphasize that this is not a fair comparison since we have used priors from WMAP7 on the secondary cosmological parameters n_s , h and $\Omega_b h^2$, but not on Ω_m or σ_8 (see Paper II for the case with no priors on n_s , h and $\Omega_b h^2$).

Fig. 4 shows the one-dimensional (histograms) and joint

two-dimensional (contour plots) marginalized posterior distributions on all five cosmological parameters. Solid contours indicate the 68% and 95% CLs obtained from the analysis presented here, while the dotted contours are the 68% and 95% CLs from the WMAP7 analysis, shown for comparison. The strongest parameter degeneracies are between Ω_m and σ_8 (cross-correlation coefficient $r = -0.81$), between $\Omega_b h^2$ and n_s ($r = 0.79$), and between Ω_m and h ($r = -0.74$). All other combinations are only weakly correlated with $|r| < 0.5$.

Overall, there is good agreement between our con-

straints and those inferred from the WMAP7 data (see also Table 4). However, there is some tension regarding the secondary cosmological parameters, which is evident from the fact that the posterior and prior distributions (indicated by red, solid curves) reveal an offset. This is most pronounced for the Hubble parameter h ; whereas the WMAP7 prior used has $h = 0.710^{+0.050}_{-0.049}$ our posterior distribution has $h = 0.739^{+0.044}_{-0.041}$ (both 95% CL). For comparison, the revised parallaxes for Cepheid stars by van Leeuwen et al. (2007) raises the value for h from the HST Key Project from $0.72 \pm 0.08 \text{ km s}^{-1} \text{ Mpc}^{-1}$ (Freedman et al. 2001) to $0.76 \pm 0.08 \text{ km s}^{-1} \text{ Mpc}^{-1}$ (68% CL), and the Cepheid-based determination of Sandage et al. (2006) from $0.62 \pm 0.05 \text{ km s}^{-1} \text{ Mpc}^{-1}$ to $0.70 \pm 0.05 \text{ km s}^{-1} \text{ Mpc}^{-1}$ (68% CL). Hence, despite some tension with the WMAP7 based constraints, our posterior distribution for the Hubble constant is well within the range of values inferred from Cepheids. Interestingly, our constraint on h is correlated with the constraints on both Ω_m and σ_8 : according to our analysis, a relatively low Hubble parameter of $h \sim 0.7$ implies $\Omega_m \sim 0.30$ and $\sigma_8 \sim 0.73$, while for $h \sim 0.78$ the results presented here suggest that $\Omega_m \sim 0.25$ and $\sigma_8 \sim 0.82$. Clearly, an improved constraint for the Hubble parameter could help to significantly tighten the constraints on both Ω_m and σ_8 .

5.2 Nuisance parameters

As discussed in §3.6, our model contains two nuisance parameters: ψ , which enters in the description of the scale dependence of the halo bias, and η , which sets the normalization of the halo concentration-mass relation. As discussed in detail in Paper I, the freedom in η also characterizes model uncertainties arising from our oversimplifications regarding the structure of dark matter haloes.

The upper panels of Fig. 5 show the posterior distributions for η (left-hand) and ψ (right-hand) of our **Fiducial** model. The contours in the other panels show 68% and 95% confidence levels of the joint two-dimensional marginalized posteriors with Ω_m and σ_8 . Clearly, neither η nor ψ shows significant correlation with Ω_m or σ_8 (in all cases the cross-correlation coefficient $|r| < 0.3$). As already discussed in Paper II, this is an important result, as it indicates that the uncertainties in the scale dependence of the halo bias and the oversimplifications regarding the structure of dark matter haloes do not have a significant impact on the cosmological constraints presented here.

The solid, red curves in the upper panels of Fig. 5 reflect the Gaussian priors that we imposed on our model. In the case of η , the posterior distribution ($\eta = -0.04^{+0.13}_{-0.11}$, 95% CL) is significantly narrower than the prior distribution ($\eta = 0.0^{+0.2}_{-0.2}$, 95% CL), indicating that the prior did not have a significant impact on our results. In the case of ψ , however, the posterior distribution ($\psi = 1.12^{+0.20}_{-0.12}$, 95% CL) is clearly offset from the prior ($\psi = 0.90^{+0.30}_{-0.30}$, 95% CL) to larger values. This might raise concern that a less restrictive prior might have resulted in significantly different cosmological constraints. However, this is not the case for the following two reasons. First, as already mentioned above, and discussed in more detailed in Paper II, ψ is only very poorly correlated with the cosmological parameters. Second, as discussed in the Appendix, when ψ increases the radial

bias function $\zeta(r, z)$ asymptotes to the empirical fitting function of Tinker et al. (2005). In other words, once ψ increases beyond a certain value, any further increase has zero impact. For the best-fit cosmology of our **Fiducial** model, this critical value of ψ is ~ 1.5 .

5.3 The Galaxy-Dark Matter Connection

One of the powerful aspects of the method used here, is that the data is used to simultaneously constrain cosmology and halo occupation statistics. Fig. 6 shows the one-dimensional (histograms) and joint two-dimensional (contour plots) marginalized posterior distributions of model **Fiducial** for the nine CLF parameters that describe the relation between galaxy luminosity and halo mass. The medians and 95% CLs are also listed in Table 5. All nine parameters are tightly constrained, with tight degeneracies between the parameters b_0 , b_1 and b_2 , that describe the normalization of the satellite CLF (see Eq. [9]), and between the parameters L_0 , M_1 and γ_1 , that describe the relation between halo mass and the luminosity of its central galaxy (see Eq. [6]).

The constraint on the faint-end slope of the satellite CLF is $\alpha_s = -1.18 \pm 0.05$ (95% CL), in good agreement with results obtained from galaxy group catalogues (e.g., Eke et al. 2004; Yang et al. 2008). The constraints on the scatter in the CLF of central galaxies is $\sigma_c = 0.157 \pm 0.007$ (95% CL), which is in excellent agreement with a variety of other constraints, from satellite kinematics (More et al. 2009), from clustering and lensing (Cacciato et al. 2009; Moster et al. 2010), and from galaxy group catalogues (Yang et al. 2008). Interestingly, such an amount of scatter is also in excellent agreement with predictions from semi-analytical models for galaxy formation (e.g., Wang et al. 2006; see also More et al. 2009).

In the left-hand panel of Fig. 7 we compare the constraints on the L_c - M relation of our **Fiducial** model (shaded area, indicating the 68% confidence region) to the results obtained by Yang et al. (2008) from the SDSS galaxy group catalogue (symbols with errorbars indicating the 68% confidence level). Here we have converted the group masses listed in their Table 1 to our definition of halo mass and the cosmology of the best-fit **Fiducial** model using the abundance matching technique described in Eq. (15) of Yang et al. (2007). Finally, the right-hand panel of Fig. 7 compares the satellite fractions as function of galaxy luminosity obtained from our **Fiducial** model (blue shaded area, indicating the 68% CL) to constraints obtained by Cooray (2006; black, open squares), Yang et al. (2008; red, open circles), van den Bosch et al. (2007; green shaded area, indicating the 68% CLs), and Tinker et al. (2007; orange shaded area, indicating the 68% CL). All these constraints are obtained comparing halo occupation models to data from the SDSS or 2dFGRS, and are in excellent agreement with each other and with the constraints from our **Fiducial** model.

Based on all these comparisons, we conclude that the constraints on the galaxy-dark matter connection for our **Fiducial** model are in excellent agreement with a wide variety of independent constraints. We emphasize that, contrary to many other studies, our combined analysis of abundance, clustering, and lensing of galaxies also accounts for uncertainties in cosmological parameters. This strongly supports

Table 4. Constraints on Cosmological Parameters

Model	Ω_m	σ_8	h	n_s	$100\Omega_b h^2$
(1)	(2)	(3)	(4)	(5)	(6)
Fiducial	$0.278^{+0.023}_{-0.026}$	$0.763^{+0.064}_{-0.049}$	$0.739^{+0.044}_{-0.041}$	$0.978^{+0.026}_{-0.025}$	$2.279^{+0.112}_{-0.107}$
Radial	$0.279^{+0.025}_{-0.026}$	$0.761^{+0.061}_{-0.049}$	$0.738^{+0.042}_{-0.043}$	$0.977^{+0.025}_{-0.026}$	$2.279^{+0.103}_{-0.110}$
Poisson	$0.280^{+0.023}_{-0.023}$	$0.744^{+0.056}_{-0.047}$	$0.741^{+0.043}_{-0.040}$	$0.980^{+0.026}_{-0.026}$	$2.287^{+0.111}_{-0.109}$
noRSSD	$0.263^{+0.026}_{-0.031}$	$0.805^{+0.083}_{-0.061}$	$0.727^{+0.054}_{-0.042}$	$0.977^{+0.030}_{-0.027}$	$2.278^{+0.117}_{-0.112}$
noSGW	$0.282^{+0.026}_{-0.026}$	$0.727^{+0.054}_{-0.049}$	$0.739^{+0.042}_{-0.040}$	$0.979^{+0.025}_{-0.023}$	$2.286^{+0.102}_{-0.101}$
WMAP7	$0.264^{+0.064}_{-0.049}$	$0.801^{+0.059}_{-0.058}$	$0.710^{+0.050}_{-0.049}$	$0.963^{+0.029}_{-0.028}$	$2.257^{+0.120}_{-0.113}$

The cosmological constraints for the various models discussed in the text (see also Table 3). Values indicate the median and 95% CLs of the marginalized posterior distributions obtained from our MCMCs. For comparison, the final row lists the constraints obtained from the WMAP7 analysis of the CMB (taken from Komatsu et al. 2011).

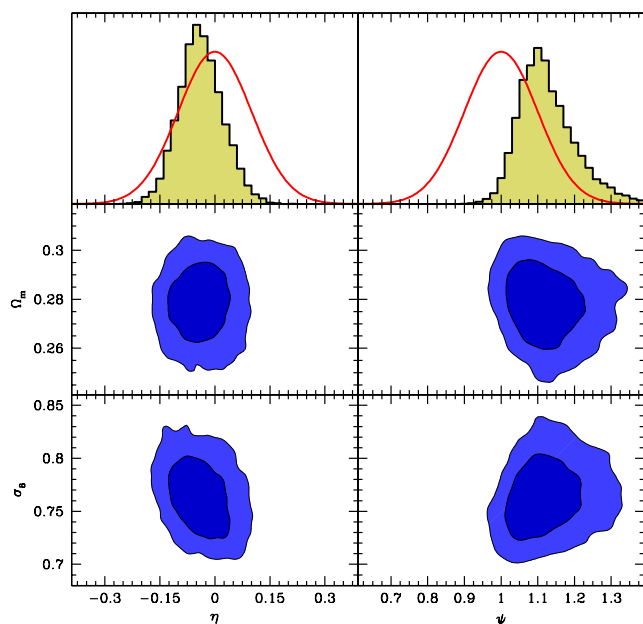


Figure 5. The shaded histograms in the upper panels show the marginalized posterior distributions for the two nuisance parameters η (left-hand panel), which sets the normalization of the halo concentration-mass relation, and ψ (right-hand panel), which enters in the description of the scale dependence of the halo bias. The solid, red curves show the corresponding Gaussian prior distributions. The contour plots in the middle and lower panels show the joint, two-dimensional marginalized posterior distributions of Ω_m and η (middle left-hand panel), σ_8 and η (lower left-hand panel), Ω_m and ψ (middle right-hand panel) and σ_8 and ψ (lower right-hand panel). See §5.2 for a detailed discussion.

that our method of simultaneously constraining cosmology and halo occupation statistics yields reliable results.

6 SYSTEMATICS

The **Fiducial** model, discussed in the previous section, relies on two assumptions regarding satellite galaxies that may not be entirely accurate. These concern the radial number density distribution of satellites and the Poisson nature of the satellite occupation numbers. In this section we gauge the impact of these assumptions on our results. In addition,

we also address the importance of properly accounting for the residual redshift space distortions present in the projected correlation functions used to constrain the models. We do so by running a series of MCMCs in which we include small variations with respect to our **Fiducial** model. These models, and their respective χ^2 -values for the best-fit model in the chain, are listed in Table 3, while the cosmological constraints are summarized in Table 4.

6.1 Radial Number Density Profile of Satellites

In our **Fiducial** model we have assumed that the radial number density distribution of satellite galaxies in a halo of mass M follows an NFW profile with a concentration parameter that is identical to that of the dark matter density profile, i.e., we assumed that $u_s(r|M) = u_h(r|M)$ (see §3.4). This has observational support from a number of studies of the radial distribution of satellite galaxies in groups and clusters (e.g., Beers & Tonry 1986; Carlberg, Yee & Ellingson 1997a; van der Marel et al. 2000; Biviano & Girardi 2003; Lin, Mohr & Stanford 2004; van den Bosch et al. 2005b; Sheldon et al. 2009).

However, a number of recent studies have argued that the spatial distribution of satellite galaxies is less centrally concentrated than the dark matter (e.g., Yang et al. 2005; Chen 2008; More et al. 2009). Interestingly, an opposite result has been obtained for luminous red galaxies (e.g., Masjedi et al. 2006; Watson et al. 2010, 2012; Tal, Wake & van Dokkum 2012). In fact, there are indications that the radial distribution of satellite galaxies appears to have some dependence on the color and/or morphologies of the central (e.g., Lorrimer et al. 1994; Sales & Lambas 2005; Lares, Lambas & Dominguez 2011; Guo et al. 2012). From a theoretical point of view, one expects the radial distribution of satellite galaxies to reflect that of dark matter subhaloes. Numerical simulations have shown that subhaloes do not follow the same spatial distribution as the dark matter; subhaloes tend to populate preferentially the outskirts of their host haloes (e.g., Diemand, Moore & Stadel 2004; Gao et al. 2004; Springel et al. 2008). However, the stellar components of satellite galaxies may be more resilient against tidal disruption than their dark matter components, such that the radial profile of satellite galaxies is not necessarily well represented by that of dark matter subhaloes in pure N -body simulations.

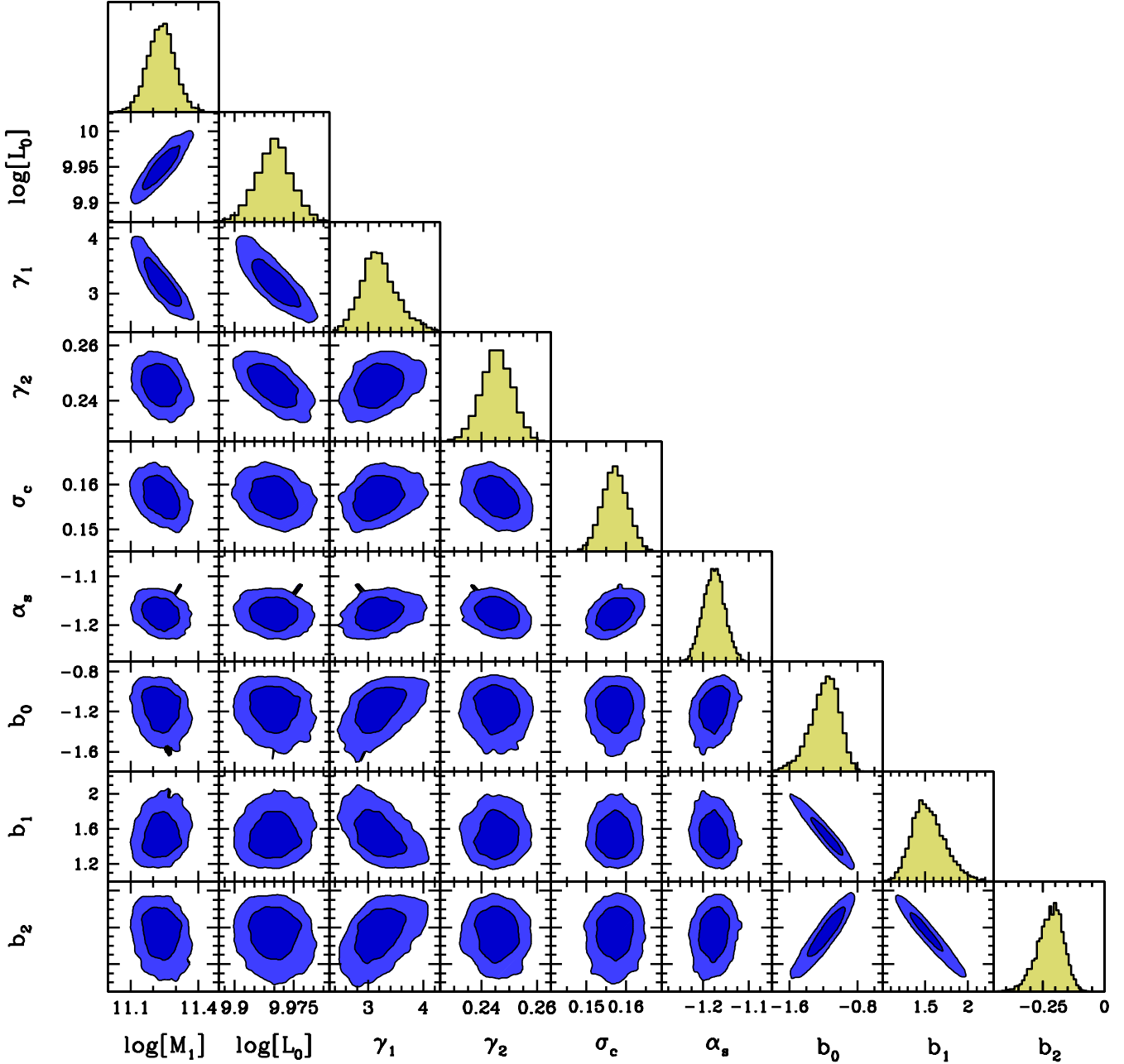


Figure 6. Constraints on the CLF parameters for the **Fiducial** model. Histograms show the marginalized posterior distributions, while the blue contour show the 68% and 95% CLs of the joint, two-dimensional marginalized posterior distributions.

In conclusion, the simple assumption that $u_s(r|M) = u_h(r|M)$ is likely oversimplified. To address the potential impact of this assumption on our results, we now consider a model in which we adopt

$$u_s(r|M) \propto \left(\frac{r}{\mathcal{R}r_*}\right)^{-1} \left(1 + \frac{r}{\mathcal{R}r_*}\right)^{-2}. \quad (44)$$

Here r_* is the scale radius of the dark matter density profile for a halo of mass M , and \mathcal{R} is a free parameter. For $\mathcal{R} = 1$ this profile reduces to that of our **Fiducial** model, i.e., $u_s(r|M) = u_h(r|M)$. Hence, \mathcal{R} is a parameter that controls how satellites are concentrated with respect to the dark matter. In order to gauge how our results depend on \mathcal{R} , and whether the data prefers values of \mathcal{R} that differ from unity,

we run a MCMC in which \mathcal{R} is a free parameter for which we adopt Gaussian prior with mean equal to unity and standard deviation, $\sigma_{\mathcal{R}} = 0.25$. In what follows we refer to this MCMC as our **Radial** model.

As is apparent from the χ^2 values of the best-fit model in the **Radial** chain (see Table 3), the extra freedom in the model does not result in a significantly better fit to the data. More importantly, the cosmological constraints are also unaffected (see upper left-hand panel of Fig. 8 and Table 4). This is also evident from the contour plots in the left-hand column of Fig. 9, which show the 68 and 95% confidence intervals of the joint two-dimensional posterior distributions for \mathcal{R} and Ω_m (middle row) and for \mathcal{R} and σ_8 (bottom row).

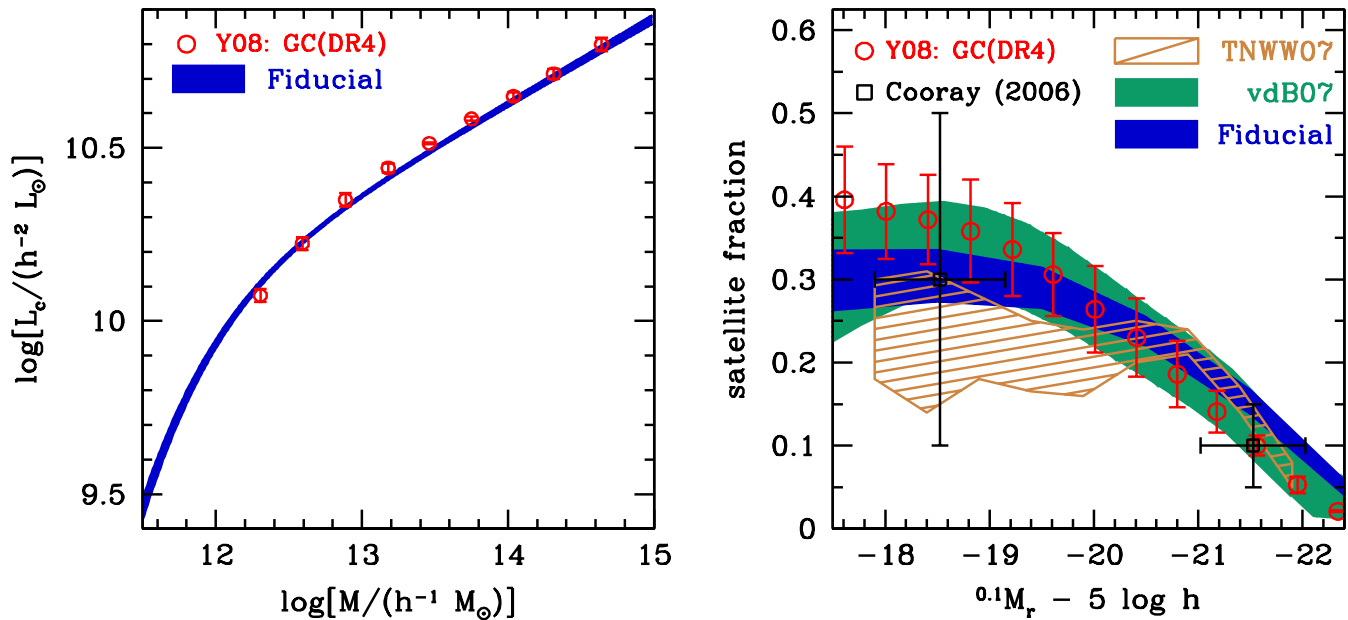


Figure 7. *Left-hand panel.* The luminosity of central galaxies, L_c , as function of halo mass, M . The shaded region indicates the 68% confidence interval for the Fiducial model, while the open red circles indicate the results of Yang et al. (2008) obtained from the SDSS group catalogue of Yang et al. (2007; error bars indicate the 68% CL), where we properly converted their group masses to our definition of halo mass and the cosmology of the best-fit Fiducial model. *Right-hand panel.* The satellite fractions as a function of r -band magnitude. The blue shaded regions indicate the 68% CL for the Fiducial model. This is compared to the satellite fractions obtained by Cooray (2006; black, open squares) from a CLF analysis of the SDSS, by Yang et al. (2008; open red circles) from the SDSS group catalogue (error bars indicate the 68% CL in both cases), by van den Bosch et al. (2007; green shaded area, indicating the 68% CL) and Tinker et al. (2007; orange shaded area, indicating the 68% CL), both from halo occupation modeling of galaxies in the 2dFGRS.

With cross-correlation coefficients $|r| < 0.1$, it is clear that neither Ω_m nor σ_8 is significantly influenced by potential uncertainty in \mathcal{R} . Finally, the histogram in the upper left-hand panel of Fig. 9 shows the posterior distribution for \mathcal{R} . With $\mathcal{R} = 0.96^{+0.32}_{-0.29}$ (95% CL) it is clear that the posterior distribution is narrower than the prior distribution (solid, red curve), and that the data prefers values of \mathcal{R} that are close to our fiducial value of unity. We conclude that our results are robust to uncertainties in the radial number density profile of satellite galaxies, and that the data used here is consistent with satellite galaxies being an unbiased tracer of the mass distribution within their host haloes (i.e., $\mathcal{R} = 1$). Interestingly, as mentioned before, this result is supported by studies of satellite galaxies in groups and clusters (e.g., Beers & Tonry 1986; Carlberg, Yee & Ellingson 1997a; van der Marel et al. 2000; Biviano & Girardi 2003; Lin, Mohr & Stanford 2004; van den Bosch et al. 2005b; Sheldon et al. 2009) but it is somewhat in disagreement with a number of studies which indicate that the radial distribution of satellite is less centrally concentrated than dark matter (e.g., Yang et al. 2005; Chen 2008; More et al. 2009). It is worth mentioning that results based on groups might be potentially affected by the offset of central galaxies (see e.g. Skibba et al. 2011). Clearly, more dedicated studies are required to further constrain the radial distribution of satellite galaxies.

6.2 Poisson Statistics of Satellite Galaxies

In our Fiducial model we have assumed that the occupation numbers of satellite galaxies obey Poisson statistics, i.e.,

$$P(N_s|M) = \frac{\langle N_s|M \rangle^{N_s} e^{-\langle N_s|M \rangle}}{N_s!}, \quad (45)$$

such that

$$\mathcal{A}_P \equiv \frac{\langle N_s(N_s - 1)|M \rangle}{\langle N_s|M \rangle^2} = 1. \quad (46)$$

As shown in Yang et al. (2008), this assumption has strong support from galaxy group catalogs. Additional support comes from numerical simulations which show that dark matter subhaloes (which are believed to host satellite galaxies) also follow Poisson statistics (e.g., Kravtsov et al. 2004). However, recently there have been several claims that the occupation statistics of subhaloes and/or satellite galaxies may deviate slightly, but significantly, from Poisson, i.e., $\mathcal{A}_P \neq 1$ (e.g., Porciani, Magliocchetti & Norberg 2004; van den Bosch et al. 2005a; Giocoli et al. 2010; Boylan-Kolchin et al. 2010; Busha et al. 2011). As shown in Paper I, the satellite-satellite term of the 1-halo power spectrum scales linearly with \mathcal{A}_P , i.e., $P_{\text{gg}}^{\text{1h}}(k) \propto \mathcal{A}_P$. Hence, any deviation of \mathcal{A}_P from unity has a direct impact on the projected correlation functions $w_p(r_p)$ on small scales, at least if the satellite-satellite term dominates over the central-satellite term (which is independent of \mathcal{A}_P).

In order to quantify how our results depend on uncertainties related to the exact form of $P(N_s|M)$, we run a

MCMC in which we include \mathcal{A}_P as a free parameter. Motivated by the empirical results of Yang et al. (2008), which suggest that the occupation statistics of satellite galaxies in the SDSS are not too different from Poisson, we adopt a Gaussian prior for \mathcal{A}_P with mean equal to unity and standard deviation, $\sigma_{\mathcal{A}_P} = 0.1$. In what follows we refer to this MCMC as our **Poisson** model.

The upper right-hand panel of Fig. 8 shows the 68 and 95% confidence levels of the joint, two-dimensional marginalized posterior distribution of Ω_m and σ_8 for model **Poisson** (yellow contours), compared to that for our **Fiducial** model (blue contours). As is evident, the extra freedom in \mathcal{A}_P results in a best-fit value for σ_8 that is slightly lower than for the **Fiducial** model (see Table 4), but the change is only marginally significant (i.e., $< 1\sigma$).

The marginalized posterior distribution for \mathcal{A}_P , shown as the shaded histogram in the upper right-hand panel of Fig. 9, has $\mathcal{A}_P = 0.88_{-0.12}^{+0.13}$ (95% CL), indicating that the data prefers a sub-Poisson probability distribution $P(N_s|M)$. The middle and bottom right-hand panels of Fig. 9 show the 68 and 95 % confidence levels of the joint, two-dimensional posterior distributions for \mathcal{A}_P and Ω_m (middle row) and for \mathcal{A}_P and σ_8 (bottom row). Whereas Ω_m is found to be completely independent of \mathcal{A}_P , there is a weak, positive correlation between \mathcal{A}_P and σ_8 (cross-correlation coefficients $r \simeq 0.3$). Hence, if we would have adopted a less restrictive prior on \mathcal{A}_P the data most likely would have preferred an even smaller value for σ_8 . We emphasize, though, that our prior has both empirical and theoretical motivation. Nevertheless, it is clear that tighter constraints on σ_8 require a more accurate assessment of the (non)-Poisson nature of $P(N_s|M)$.

6.3 Residual Redshift Space Distortions

In §3.5 we have shown that, when computing the projected galaxy correlation functions, we use a modified form of the ‘Kaiser’ formalism (Kaiser 1987) to account for the residual redshift space distortions (hereafter RRSD) present in the data. These RRSD arise as a consequence of the fact that the line-of-sight projection was only performed out to a distance of $r_{\max} = 40h^{-1}$ Mpc or $60h^{-1}$ Mpc (depending on the magnitude bin, see Table 2). In Paper I, we have shown that not taking this correction into account results in systematic errors that can easily exceed 20 percent on scales above ~ 10 Mpc. In this section, we show how not correcting for RRSD can bias the inference of cosmological parameters such as Ω_m and σ_8 . To this aim, we run a MCMC in which we compute the projected galaxy correlation function without correcting for RRSD, i.e., we use

$$w_p(r_p) = 2 \int_{r_p}^{r_{\text{out}}} \xi_{\text{gg}}(r) \frac{r dr}{\sqrt{r^2 - r_p^2}}, \quad (47)$$

with $r_{\text{out}} = \sqrt{r_p^2 + r_{\max}^2}$. As discussed in Paper I, this is the standard method used by numerous authors in the past (e.g., Zehavi et al. 2004, 2005, 2011; Abazajian et al. 2005; Tinker et al. 2005; Zheng et al. 2007, 2009; Yoo et al. 2009). In what follows we refer to this MCMC as our **noRRSD** model.

The lower left-hand panel of Fig. 8 shows the 68% and 95% confidence levels of the joint, two-dimensional marginalized posterior distribution of Ω_m and σ_8 for model **noRRSD**

(yellow contours), compared to that for our **Fiducial** model (blue contours). As is evident, not correcting for the RRSD biases σ_8 high by $\sim 6\%$ and Ω_m low by about $\sim 5\%$ (cf. Table 4). Although this systematic bias is only at the $\sim 1\sigma$ level for the current data, its significance will increase when using more accurate data and/or data that extends to larger radii. Hence, we conclude that, in this era of precision cosmology, properly correcting for RRSD is important.

6.4 Sample Variance

Even with a survey the size of SDSS, it is important to address the issue of sample variance. This requires full covariance matrices for the entire data set (including the covariance between the LF, WP and ESD data), and requires large numbers of realistic mock catalogs. This in turn requires a large suite of very large and high resolution N -body simulations, which we, unfortunately, do not have available at this stage. An alternative is to use jackknife or bootstrap estimates for the covariance matrix, which can be constructed from the data itself. Although these fail to account for sample variance on the scale of the survey itself, parameter uncertainties estimated from jackknife errors are likely to be conservative (Norberg et al. 2011). Unfortunately, since we do not have access to the galaxy-galaxy lensing data products, we cannot construct such a jackknife covariance matrix. We have recently started a project to perform our own analysis of the galaxy-galaxy lensing signal in the SDSS, following a method similar to that of Mandelbaum et al. (2005, 2006). Once completed, we will use those data together with our own measurements of the clustering and luminosity (or stellar mass) functions (see Yang et al. 2012), to construct a full covariance matrix for our data set using jackknife or bootstrap estimates.

In this study, however, we have ignored sample variance in our analysis, and we caution that our error estimates for the model parameters are therefore likely to be underestimated. However, we can still perform a simple test to gauge the potential impact of sample variance on our results. As already alluded to in §5, the most important manifestation of sample variance in the SDSS appears to be the Sloan Great Wall (SGW). In order to get a rough estimate of how the presence or absence of the SGW in our data sample impacts on the cosmological constraints, we perform the following exercise. We construct a MCMC using the same ingredients and priors as for our fiducial model, but we exclude the $w_p(r_p)$ data for the $[-20, -21]$ magnitude bin. As shown by Zehavi et al. (2011), this is the magnitude bin that is most severely affected by the Sloan Great Wall (SGW). We refer to the resulting MCMC as model **noSGW**. The lower right-hand panel of Fig. 8 shows that excluding this part of the data lowers the value of σ_8 by $\sim 5\%$ to $\sigma_8 = 0.727_{-0.049}^{+0.054}$ (see Table 4), whereas Ω_m remains largely unaffected. Note that we only removed that subset of the $w_p(r_p)$ data that is most severely affected by the SGW, but that we did not remove the corresponding data from the ESD or LF. The cosmological constraints obtained for model **noSGW** therefore have to be interpreted with care. The main purpose of this exercise is to demonstrate that sample variance, even in a survey the size of SDSS, is still likely to be the dominant source of error in the analysis presented here.

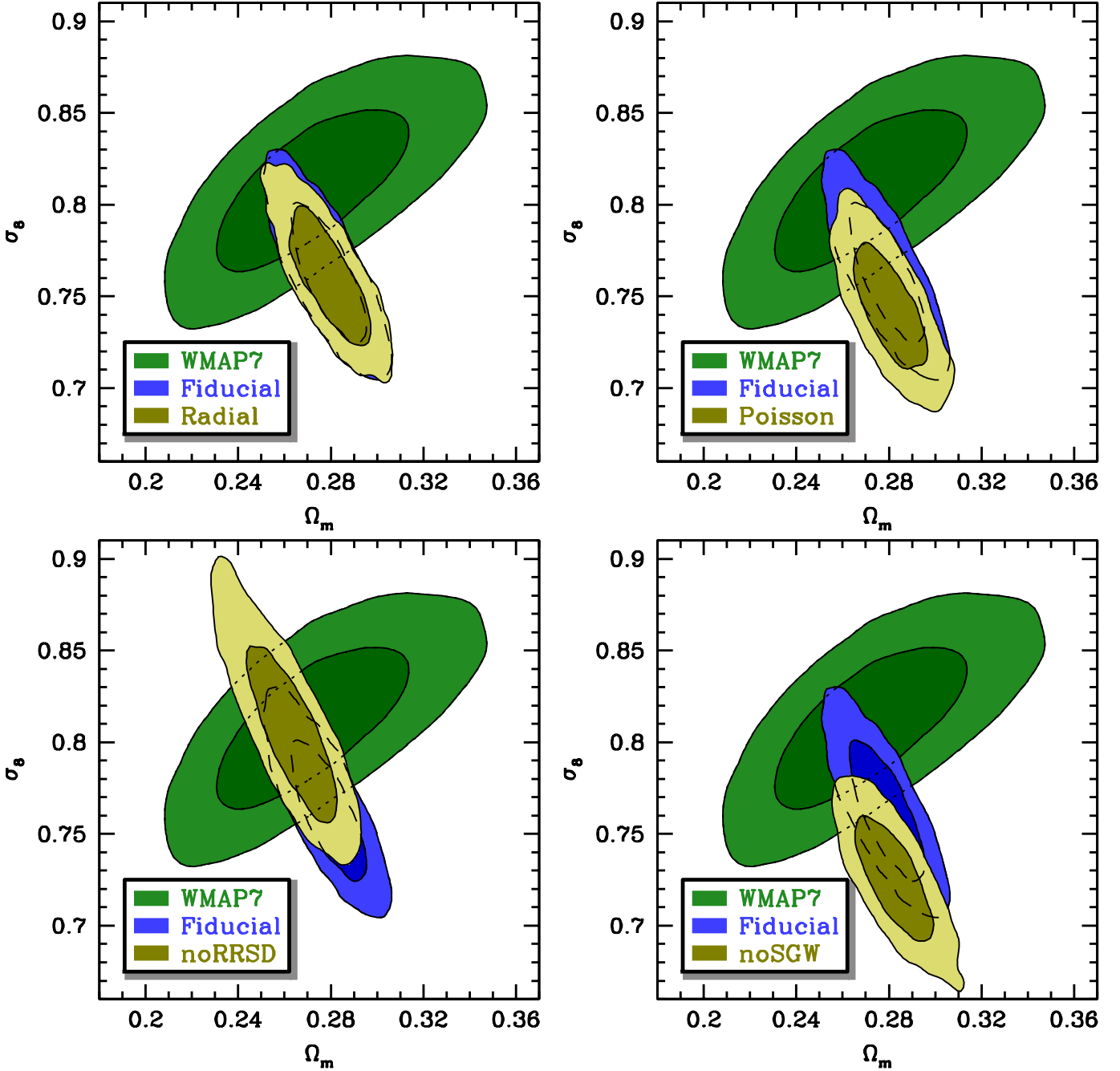


Figure 8. A comparison of the 68% and 95% CLs of the joint, two-dimensional marginalized posterior distributions of Ω_m and σ_8 for our fiducial model in blue contours and, in yellow contours, model *Radial* (upper left-hand panel), model *Poisson* (upper right-hand panel), model *noRRSD* (lower left-hand panel), and model *noSGW* (lower right-hand panel). In all panels the green contours correspond to the constraints from WMAP7, and are shown for comparison. See text for detailed discussion and Table 4 for a listing of the corresponding constraints on the cosmological parameters.

7 CONCLUSIONS

Galaxies can be observed over cosmological scales, making them useful tracers of the underlying dark matter density field. Hence, their spatial distribution is a potentially powerful probe for cosmology. Unfortunately, galaxies are biased tracers of the mass distribution, and this so-called galaxy bias depends on galaxy properties, on scale, and is even know

to be stochastic. Because of these complications, galaxy bias is generally considered a nuisance when using galaxies to constrain cosmology. However, since galaxy bias also contains a wealth of information regarding galaxy formation, it would be highly advantageous if one could *simultaneously* solve for cosmology and galaxy bias.

Several studies have used galaxy power spectra to simultaneously constrain cosmology and galaxy bias (e.g., Cole et

Table 5. Constraints on CLF Parameters

Model	$\log(M_1)$	$\log(L_0)$	γ_1	γ_2	σ_c	α_s	b_0	b_1	b_2
(1)	(2)	(3)	(4)	(5)	(6)				
Fiducial	$11.24^{+0.12}_{-0.12}$	$9.95^{+0.05}_{-0.05}$	$3.18^{+0.80}_{-0.57}$	$0.245^{+0.011}_{-0.012}$	$0.157^{+0.007}_{-0.007}$	$-1.18^{+0.05}_{-0.05}$	$-1.17^{+0.28}_{-0.42}$	$1.53^{+0.46}_{-0.32}$	$-0.217^{+0.091}_{-0.132}$
Radial	$11.24^{+0.11}_{-0.13}$	$9.95^{+0.04}_{-0.05}$	$3.17^{+0.87}_{-0.52}$	$0.245^{+0.011}_{-0.011}$	$0.157^{+0.007}_{-0.007}$	$-1.17^{+0.05}_{-0.05}$	$-1.14^{+0.30}_{-0.55}$	$1.50^{+0.54}_{-0.31}$	$-0.212^{+0.086}_{-0.133}$
Poisson	$11.23^{+0.11}_{-0.12}$	$9.95^{+0.04}_{-0.05}$	$3.30^{+0.83}_{-0.53}$	$0.247^{+0.012}_{-0.011}$	$0.158^{+0.007}_{-0.006}$	$-1.18^{+0.05}_{-0.05}$	$-1.15^{+0.28}_{-0.38}$	$1.52^{+0.43}_{-0.33}$	$-0.210^{+0.095}_{-0.117}$
noRSSD	$11.23^{+0.11}_{-0.13}$	$9.96^{+0.04}_{-0.05}$	$3.00^{+0.78}_{-0.45}$	$0.239^{+0.012}_{-0.012}$	$0.158^{+0.007}_{-0.007}$	$-1.17^{+0.05}_{-0.05}$	$-1.28^{+0.32}_{-0.46}$	$1.68^{+0.51}_{-0.36}$	$-0.262^{+0.099}_{-0.132}$
noSGW	$11.02^{+0.16}_{-0.10}$	$9.86^{+0.06}_{-0.04}$	$4.77^{+0.75}_{-1.18}$	$0.273^{+0.014}_{-0.015}$	$0.142^{+0.010}_{-0.009}$	$-1.01^{+0.11}_{-0.12}$	$-0.64^{+0.23}_{-0.45}$	$1.17^{+0.41}_{-0.27}$	$-0.208^{+0.093}_{-0.108}$

Constraints on the CLF parameters for the various models discussed in the text (see also Table 3). Values indicate the median and 95% CLs of the marginalized posterior distributions obtained from our MCMCs.

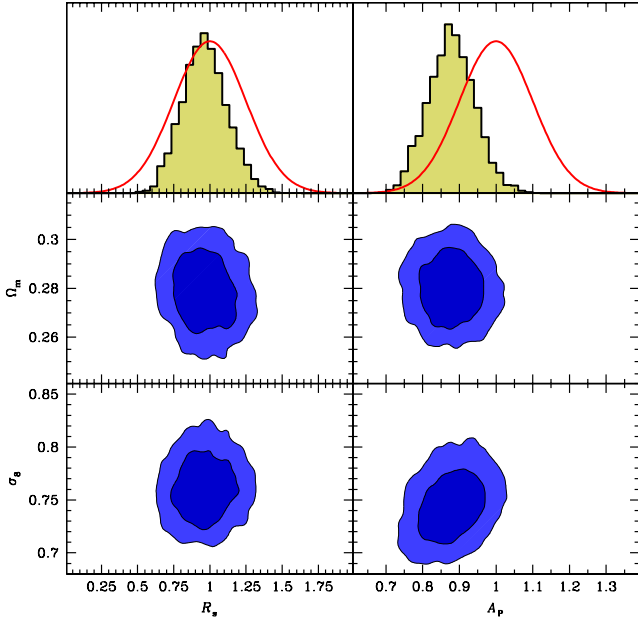


Figure 9. The shaded histograms in the upper panels show the marginalized posterior distributions for the parameter \mathcal{R} (left-hand panel), which controls the radial distribution of satellite galaxies (see Eq. [44]), and \mathcal{A}_p (right-hand panel), which describes deviations of the satellite occupation distribution from a Poisson distribution (see Eq. [46]). The solid, red curves show the corresponding Gaussian prior distributions used in models *Radial* and *Poisson*, respectively. The contour plots in the middle and lower panels show the joint, two-dimensional marginalized posterior distributions of Ω_m and \mathcal{R} (middle left-hand panel), σ_8 and \mathcal{R} (lower left-hand panel), Ω_m and \mathcal{A}_p (middle right-hand panel) and σ_8 and \mathcal{A}_p (lower right-hand panel). See §6.1 and §6.2 for details.

al. 2005; Tegmark et al. 2006; Padmanabhan et al. 2007). These studies, however, often resulted in tension regarding the cosmological matter density, Ω_m . This is likely to be a consequence of the fact that these studies used a poorly motivated, inaccurate fitting function for the scale-dependence of the galaxy bias due to non-linearity, causing biased estimates of the cosmological parameters (e.g., Sánchez & Cole 2008; Yoo et al. 2009; Hamann et al. 2008). This indicates that it is prudent to use a realistic, physically motivated model for the galaxy bias.

In this paper we have simultaneously constrained cosmology and galaxy bias using measurements of galaxy abun-

dances, galaxy clustering and galaxy-galaxy lensing, all taken from the SDSS. We used a realistic, accurate and intuitive model for galaxy bias, based on the conditional luminosity function (which describes the halo occupation statistics as function of galaxy luminosity) combined with the halo model (which describes the non-linear matter field in terms of its halo building blocks). We improved on previous, similar studies (e.g., Seljak et al. 2005; Cacciato et al. 2009) by (i) using a more accurate analytical model, (ii) using the latest clustering data, (iii) correcting the latter for residual redshift space distortions, and (iv) marginalizing over uncertainties related to the detailed structure of dark matter haloes.

As detailed in Paper I (van den Bosch et al. 2012), our model, which includes scale-dependence of the halo bias and a proper treatment of halo exclusion, reproduces the 3-dimensional galaxy-galaxy correlation and the galaxy-matter cross-correlation (which can be projected to predict the observables) with an accuracy better than 10 (in most cases 5) percent. Since this uncertainty is not systematic, the accuracy is expected to be much better for the projected galaxy-galaxy correlation function and the galaxy-galaxy lensing signal, which are the observed quantities. Furthermore, although we believe the halo mass function and halo bias function, $n(M, z)$ and $b_h(M, z)$, obtained by Tinker et al. (2008, 2010) to be the most accurate to date, it is important to realize that they still can carry uncertainties that can potentially impact the results on cosmological parameters. It is unclear if such uncertainties affect just the mass function normalization and not its shape. We intend to carry out a proper investigation of this issue in future work. Throughout this paper, we restrict ourselves to the $n(M, z)$ and $b_h(M, z)$ specified above.

In order to constrain our model parameters, we have adopted a full Bayesian framework in which we use Monte Carlo Markov Chains (MCMC) to probe the posterior distributions. Under the assumption of a spatially flat, vanilla Λ CDM cosmology, and using WMAP7 priors on the secondary cosmological parameters, $(n_s, h, \Omega_b h^2)$, we obtain that $\Omega_m = 0.278^{+0.023}_{-0.026}$ and $\sigma_8 = 0.763^{+0.064}_{-0.049}$ (both 95% CL). These are among the tightest constraints on these two cosmological parameters ever obtained, and are perfectly consistent with the constraints from WMAP7 (Komatsu et al. 2011). We emphasize that no priors were used for either Ω_m or σ_8 . Our analysis, which uses a realistic model for galaxy bias, therefore demonstrates that the observed distribution of galaxies, down to the smallest non-linear scales,

is perfectly consistent with the vanilla Λ CDM cosmology, and that the use of a realistic and accurate model for galaxy bias removes the tension between the spatial distribution of galaxies and the CMB anisotropies that hampered previous studies based on galaxy power spectra.

In order to assess the robustness of our results, we have performed a number of tests in which we relaxed some of our model assumptions. In particular, we have shown that the cosmological constraints are extremely robust to assumptions regarding the radial number density profile of satellite galaxies, and that the data is perfectly consistent with satellite galaxies being an unbiased tracer of the mass distribution within their host haloes. Our results are also robust to assumptions regarding the second moment of the satellite occupation distribution, $P(N_s|M)$. In our fiducial model we have made the customary assumption that $P(N_s|M)$ follows a Poisson distribution. Relaxing this assumption lowers the best-fit value for σ_8 by $\sim 2.5\%$ ($\sim 1\sigma$), to $\sigma_8 = 0.744^{+0.056}_{-0.047}$, while the constraints on Ω_m remain almost identical. Interestingly, the data seems to have a slight (marginally significant) preference for a $P(N_s|M)$ that is sub-Poisson (i.e., for which $\langle N_s(N_s - 1)|M \rangle < \langle N_s|M \rangle^2$), consistent with expectations based on the occupation statistics of (massive) dark matter subhaloes (e.g., Kravtsov et al. 2004; Boylan-Kolchin et al. 2010).

We have also shown that not correcting the projected correlation functions of Zehavi et al. (2011) for residual redshift space distortions biases σ_8 high and Ω_m low, both by $\sim 5\%$. Hence, in this era of precision cosmology, correcting for these RRS D cannot be neglected. Fortunately, as demonstrated in Paper I, RRS D can be corrected for in a straightforward and accurate manner using a slightly modified version of the Kaiser (1987) formalism.

The Bayesian analysis presented here has not accounted for sample variance. We have performed a simple, naive test to gauge the potential impact of sample variance, by excluding part of the clustering data that samples the SGW, the largest coherent structure detected in the SDSS. This lowers the value of σ_8 by $\sim 5\%$ ($\sim 1\sigma$) compared to the fiducial model, to $\sigma_8 = 0.727^{+0.054}_{-0.049}$, whereas Ω_m remains largely unaffected. Hence, we conclude that sample variance may well be the dominant source of uncertainty for our results. We have recently started to develop our own pipeline to measure the galaxy-galaxy lensing signal in the SDSS, which we will use to estimate the full covariance for our data set using jackknife or bootstrap sampling. This will allow us to better address the issue of sample variance for the results presented here.

8 ACKNOWLEDGMENTS

The work presented in this paper has greatly benefited from discussions with Alexie Leauthaud, Rachel Mandelbaum, Jeremy Tinker, Risa Wechsler, Idit Zehavi and Zheng Zheng. MC acknowledges support from the German-Israeli Foundation (GIF) I-895-207.7/2005, and from the Minerva Fellowship (by Max Planck Gesellschaft). FvdB acknowledges support from the Lady Davis Foundation for a Visiting Professorship at Hebrew University. This research was supported in part by the National Science Foundation under Grant No. NSF PHY11-25915 and NSF PHY-0551142.

REFERENCES

- Abazajian K., et al., 2005, *ApJ*, 625, 613
 Abazajian K., et al., 2009, *ApJS*, 182, 543
 Adelman-McCarthy J.K., et al., 2006, *ApJS*, 162, 38
 Astier P., et al., 2006, *A&A*, 447, 31
 Balbi A., et al., 2000, *ApJ*, 545, 1
 Baldauf T., Smith R.E., Seljak U., Mandelbaum R., 2010, *Phys. Rev. D*, 81, 063531
 Beers T.C., Tonry J.L., 1986, *ApJ*, 300, 557
 Benjamin J., et al., 2007, *MNRAS*, 381, 702
 Benson B.A., et al., 2011, preprint (arXiv:1112.5435)
 Berlind A.A., Weinberg D.H., 2002, *ApJ*, 575, 587
 Biviano A., Girardi M., 2003, *ApJ*, 585, 205
 Blanton M.R., et al. 2003a, *ApJ*, 592, 819
 Blanton M.R., et al. 2003b, *AJ*, 125, 2348
 Boylan-Kolchin M., Springel V., White S.D.M., Jenkins A., 2010, *MNRAS*, 406, 896
 Bullock J.S., Kolatt T.S., Sigad Y., Somerville R.S., Kravtsov A.V., Klypin A.A., Primack J.R., Dekel A., 2001, *MNRAS*, 321, 559
 Burles S., Nollett K.M., Turner M.S., 2001, *ApJ*, 552, 1
 Busha M.T., Wechsler R.H., Behroozi P.S., Gerke B.F., Klypin A.A., Primack J.R., 2011, *ApJ*, 743, 11
 Cacciato M., van den Bosch F.C., More S., Li R., Mo H.J., Yang X., 2009, *MNRAS*, 394, 929
 Cacciato M., Lahav O., van den Bosch F.C., Hoekstra H., Dekel A., 2012, preprint (arXiv:1203.2616)
 Carlberg R.G., Yee H.K.C., Ellingson E., 1997, *ApJ*, 478, 462
 Chen J., 2008, *A&A*, 384, 347
 Cole S., et al., 2005, *MNRAS*, 362, 505
 Colless M., et al., 2003, preprint (arXiv:astro-ph/0306581)
 Cooray A., 2006, *MNRAS*, 365, 842
 Cooray A., Sheth R.K., 2002, *Phys. Rep.*, 372, 1
 Dekel A., Lahav O., 1999, *ApJ*, 520, 24
 Desjacques V., Nusser A., 2005, *MNRAS*, 361, 1257
 Diemand J., Moore B., Stadel J., 2004, *MNRAS*, 352, 535
 Dunkley J., et al., 2009, *ApJS*, 180, 306
 Eisenstein D.J., Hu W., 1998, *ApJ*, 496, 605
 Eke V.R., Navarro J.F., Steinmetz M., 2001, *ApJ*, 554, 114
 Eke V.R., et al. (The 2dFGRS team), 2004, *MNRAS*, 355, 769
 Freedman W.L., et al., 2001, *ApJ*, 553, 47
 Fu L., et al., 2008, *A&A*, 479, 9
 Gao L., White S.D.M., Jenkins A., Stoehr F., Springel V., 2004, *MNRAS*, 355, 819
 Giannantonio T., Scranton R., Crittenden R.G., Nichol R.C., Boughn S.P., Myers A.D., Richards G.T., 2008, *Phys. Rev. D*, 77, 123520
 Giocoli C., Tormen G., Sheth R.K., van den Bosch F.C., 2010, *MNRAS*, 404, 502
 Gott J.R., Juric M., Schlegel D.J., Hoyle F., Vogeley M.S., Tegmark M., Bahcall N.A., Brinkmann J., 2005, *ApJ*, 624, 463
 Guzik J., Seljak U., 2002, *MNRAS*, 325, 311
 Guo Q., Cole S., Eke V., Frenk C., 2012, preprint (arXiv:1201.1296)
 Guzzo L., et al., 2000, *A&A*, 355, 1
 Hamann J., Hannestad S., Melchiorri A., Wong Y.Y., 2008, *JCAP*, 07, 017
 Hastings W.K., 1970, *Biometrika*, 57, 97
 Ho S., Hirata C.M., Padmanabhan N., Seljak U., Bahcall N., 2008, *Phys. Rev. D*, 78, 043519
 Jing Y.P., Mo H.J., Börner G., 1998, *ApJ*, 503, 37
 Kaiser N., 1987, *MNRAS*, 227, 1
 Komatsu E., et al., 2009, *ApJS*, 180, 330
 Komatsu E., et al., 2011, *ApJS*, 192, 18
 Koopmans L.V.E., Treu T., Fassnacht C.D., Blandford R.D., Surpi G., 2003, *ApJ*, 599, 70

- Kowalski M., et al., 2008, *ApJ*, 686, 749
- Kravtsov A.V., Berlind A.A., Wechsler R.H., Klypin A.A., Gottlöber S., Allgood B., Primack J.R., 2004, *ApJ*, 609, 35
- Lange A.E., et al., 2001, *Phys. Rev. D.*, 63, 042001
- Lares M., Lambas D.G., Domínguez M.J., 2011, *AJ*, 142, 13
- Li R., Mo H.J., Zuhui F., Cacciato M., van den Bosch F.C., Yang X., More S., 2009, *MNRAS*, 394, 1016
- Lin Y.-T., Mohr J.J., Stanford S.A., 2004, *ApJ*, 610, 745
- Lin H., et al., 2011, preprint (arXiv:1111.6622)
- Lorrimer S.J., Frenk C.S., Smith R.M., White S.D.M., Zaritsky D., 1994, *MNRAS*, 269, 696
- Ma C.-P., Fry J.N., 2000, *ApJ*, 543, 503
- Macciò A.V., Dutton A.A., van den Bosch F.C., Moore B., Potter D., Stadel J., 2007, *MNRAS*, 378, 55
- Mandelbaum R., et al., 2005, *MNRAS*, 368, 715
- Mandelbaum R., Seljak U., Kauffmann G., Hirata C.M., Brinkmann J., 2006, *MNRAS*, 368, 715
- Masjedi M., et al., 2006, *ApJ*, 644, 54
- Mather J.C., Fixsen D.J., Shafer R.A., Mosier C., Wilkinson D.T., 1999, *ApJ*, 512, 511
- McDonald P., et al., 2005, *ApJ*, 635, 761
- Metropolis N., Rosenbluth A.W., Rosenbluth M.N., Teller A.H., Teller E., 1953, *Chem. Phys.*, 21, 1087
- Mo H.J., White S.D.M., 1996, *MNRAS*, 282, 347
- Mo H.J., van den Bosch F.C., White S.D.M., 2010, *Galaxy Formation and Evolution*, Cambridge University Press, Cambridge
- More S., 2011, *ApJ*, 741, 19
- More S. van den Bosch F.C., Cacciato M., Mo H.J., Yang X., Li R., 2009, *MNRAS*, 392, 801
- More S. van den Bosch F.C., Cacciato M., Skibba R., Mo H.J., Yang X., 2011, *MNRAS*, 410, 210
- More S. van den Bosch F.C., Cacciato M., More A., Mo H.J., Yang X., 2012a, preprint (arXiv:1204.0786)
- More S. van den Bosch F.C., Cacciato M., More A., Mo H.J., Yang X., 2012b, submitted (Paper II)
- Moster B.P., Somerville R.S., Maulbetsch C., van den Bosch F.C., Maccio A.V., Naab T., Oser L., 2010, *ApJ*, 710, 903
- Navarro J.F., Frenk C.S., White S.D.M., 1997, *ApJ*, 490, 493
- Netterfield C.B., et al., 2002, *ApJ*, 571, 604
- Neyman J., Scott E.L., 1952, *ApJ*, 116, 144
- Norberg P., et al., 2001, *MNRAS*, 328, 64
- Norberg P., et al., 2002, *MNRAS*, 332, 827
- Norberg P., Baugh C.M., Gaztanaga E., Croton D.J., 2009, *MNRAS*, 396, 19
- Norberg P., Gaztanaga E., Baugh C.M., Croton D.J., 2011, *MNRAS*, 418, 2435
- Oguri M., et al., 2008, *AJ*, 135, 512
- O'Meara J.M., Burles S., Prochaska J.X., Prochter G.E., Bernstein R.A., Burgess K.M., 2006, *ApJ*, 649, L61
- Padmanabhan N., White M., Eisenstein D.J., 2007, *MNRAS*, 376, 1702
- Padmanabhan N., et al., 2007, *MNRAS*, 378, 852
- Park C., Vogeley M.S., Geller M.J., Huchra J.P., 1994, *ApJ*, 431, 569
- Peacock J.A., Smith R.E., 2000, *MNRAS*, 318, 1144
- Percival W.J., et al., 2007, *ApJ*, 657, 645
- Perlmutter S., et al., 1999, *ApJ*, 517, 565
- Porciani C., Magliocchetti M., Norberg P., 2004, *MNRAS*, 355, 1010
- Pryke C., Halverson N.W., Leitch E.M., Kovac J., Carlstrom J.E., Holzappel W.L., Dragovan M., 2002, *ApJ*, 568, 46
- Reichardt C.L., et al., 2009, *ApJ*, 694, 1200
- Reid B.A., Spergel D.N., Bode P., 2009, *ApJ*, 702, 249
- Riess A.G., et al., 1998, *AJ*, 116, 1009
- Rozo E., et al., 2010, *ApJ*, 708, 645
- Ruhl J.E., et al. 2003, *ApJ*, 599, 786
- Sales L., Lambas D.G., 2005, *MNRAS*, 356, 1045
- Sánchez A.G., Cole S., 2008, *MNRAS*, 385, 830
- Sandage A., Tammann G.A., Saha A., Reindl B., Macchett F.D., Panagia N., 2006, *ApJ*, 653, 843
- Scoccimarro R., Sheth R.K., Hui L., Jain B., 2001, *ApJ*, 546, 20
- Scott D., Srednicki M., White M., 1994, *ApJ*, 421, L5
- Seljak U., 2000, *MNRAS*, 318, 203
- Seljak U., et al., 2005, *Phys. Rev. D*, 71, 043511
- Sheldon E.S., et al., 2009, *ApJ*, 703, 2232
- Skibba R. A., van den Bosch F. C., Yang X., More S., Mo H., Fontanot F., 2011, *MNRAS*, 410, 417
- Smith R.E., et al., 2003, *MNRAS*, 341, 1311
- Spergel D.N., et al., 2003, *ApJS*, 148, 175
- Spergel D.N., et al., 2007, *ApJS*, 170, 377
- Springel V., et al., 2008, *MNRAS*, 391, 1685
- Tal T., Wake D.A., van Dokkum P.G., 2012, *ApJ*, 751, 5
- Tal T., Wake D.A., van Dokkum P.G., van den Bosch F.C., Schneider D.P., Brinkman J., Weaver B.A., 2012, *ApJ*, 746, 138
- Tegmark M., Bromley B.C., 1999, *ApJ*, 518, 69
- Tegmark M., et al., 2006, *Phys. Rev. D.*, 74, 123507
- Tinker J.L., Weinberg D.H., Zheng Z., Zehavi I., 2005, *ApJ*, 631, 41
- Tinker J.L., Norberg P., Weinberg D.H., Warren M.S., 2007, *ApJ*, 659, 877
- Tinker J.L., Kravtsov A.V., Klypin A., Abazajian K., Warren M., Yepes G., Gottlöber S., Holz D.E., 2008, *ApJ*, 688, 709
- Tinker J.L., Robertson B.E., Kravtsov A.V., Klypin A., Warren M., Yepes G., Gottlöber S., 2010, *ApJ*, 724, 878
- Tinker J.L., et al., 2012, *ApJ*, 745, 16
- van den Bosch F.C., Yang X., Mo H.J., 2003a, *MNRAS*, 340, 771
- van den Bosch F.C., Mo H.J., Yang X., 2003b, *MNRAS*, 345, 923
- van den Bosch F.C., Tormen G., Giocoli C., 2005a, *MNRAS*, 359, 1029
- van den Bosch F.C., Yang X., Mo H.J., Norberg P., 2005b, *MNRAS*, 356, 1233
- van den Bosch F.C., Yang X., Mo H.J., Weinmann S.M., Maccio A.V., More S., Cacciato M., Skibba R., Kang, X., 2007, *MNRAS*, 376, 841
- van den Bosch F.C., More S., Cacciato M., Mo H.J., Yang X., 2012, preprint (arXiv:1206.6890), (Paper I)
- van der Marel R.P., Magorrian J., Carlberg R.G., Yee H.K.C., Ellingson E., 2000, *AJ*, 119, 2038
- van Leeuwen F., Feast M.W., Whitelock P.A., Laney C.D., 2007, *MNRAS*, 379, 723
- Viel M., Weller J., Haehnelt M.G., 2004, *MNRAS*, 355, L23
- Vikhlinin A., et al., 2009, *ApJ*, 692, 1060
- Wang L., Li C., Kauffmann G., De Lucia G., 2006, *MNRAS*, 371, 537
- Wang Y., Yang X., Mo H.J., van den Bosch F.C., 2007, *ApJ*, 664, 608
- Watson D.F., Berlind A.A., McBride C.K., Masjedi M., 2010, *ApJ*, 709, 115
- Watson D.F., Berlind A.A., McBride C.K., Hogg D.W., Jiang T., 2012, *ApJ*, 749, 83
- Yang X., Mo H.J., van den Bosch F.C., 2003, *MNRAS*, 339, 1057
- Yang X. Mo H.J., Jing Y.P., van den Bosch F.C., Chu Y., 2004, *MNRAS*, 350, 1153
- Yang X., Mo H.J., van den Bosch F.C., Weinmann S.M., Li C., Jing Y.P., 2005, *MNRAS*, 362, 711
- Yang X., Mo H.J., van den Bosch F.C., Pasquali A., Li C., Barden M., 2007, *ApJ*, 671, 153
- Yang X., Mo H.J., van den Bosch F.C., 2008, *ApJ*, 676, 248
- Yang X., Mo H.J., van den Bosch F.C., Zhang Y., Han J., 2012, *ApJ*, 752, 41
- Yoo J., Tinker J.L., Weinberg D.H., Zheng Z., Katz N., Davé R., 2006, *ApJ*, 652, 26
- Yoo J., Weinberg D.H., Tinker J.L., Zheng Z., Warren M.S., 2009, *ApJ*, 698, 967
- York D.G., et al., 2000, *AJ*, 120, 1579

- Zehavi I., et al., 2004, ApJ, 608, 16
 Zehavi I., et al., 2005, ApJ, 630, 1
 Zehavi I., et al., 2011, ApJ, 736, 59
 Zhao D.H., Jing Y.P., Mo H.J., Börner G., 2009, ApJ, 707, 354
 Zheng Z., Coil A., Zehavi I., 2007, ApJ, 667, 760
 Zheng Z., Zehavi I., Eisenstein D.J., Weinberg D.H., Jing Y.P., 2009, ApJ, 707, 554

depends on cosmology, we include an uncertainty of ~ 15 percent on ψ in our cosmological analysis (i.e., we treat ψ as a free ‘nuisance’ parameter, using a Gaussian prior centered on $\psi = 0.9$ and with $\sigma_\psi = 0.15$). Note that if Eq. (A5) has no solution (i.e., when ψ is sufficiently large), we set $r_\psi = 0$, which corresponds to simply using the fitting function (A3) without modification.

APPENDIX A: THE CORRELATION FUNCTION OF DARK MATTER HALOES

The function $Q(k|M_1, M_2, z)$, which enters in the 2-halo terms of the galaxy-galaxy and galaxy-matter power spectra (Eq. [17]), is related to the power spectrum of haloes of masses M_1 and M_2 at redshift z . Taking account of the large scale bias of haloes, its radial dependence (in the quasi-linear regime), and the fact that dark matter haloes have a finite extent and therefore have a minimum separation $r_{\min} = r_{\min}(M_1, M_2)$ (i.e., the so called halo exclusion), the two-point correlation function between haloes of masses M_1 and M_2 can be written as

$$1 + \xi_{\text{hh}}(r, z|M_1, M_2) = [1 + b_{\text{h}}(M_1, z) b_{\text{h}}(M_2, z) \zeta(r, z) \xi_{\text{mm}}(r, z)] \Theta(r - r_{\min}). \quad (\text{A1})$$

Here $b_{\text{h}}(M, z)$ is the linear halo bias, $\zeta(r, z)$ describes the scale dependence of the halo bias in the quasi-linear regime, and $\Theta(x)$ is the Heaviside step function, which assures that $\xi_{\text{hh}}(r, z|M_1, M_2) = -1$ for $r < r_{\min}$ in order to account for halo exclusion. Throughout we set $r_{\min} = \max[r_{200}(M_1), r_{200}(M_2)]$, in accordance with the particular halo exclusion adopted by Tinker et al. (2008,2010), whose halo mass function and halo bias function we use. As detailed in Paper I, this implies that

$$Q(k|M_1, M_2, z) \equiv 4\pi \int_{r_{\min}}^{\infty} [1 + \xi_{\text{hh}}(r, z|M_1, M_2)] \frac{\sin kr}{kr} r^2 dr, \quad (\text{A2})$$

As shown by Tinker et al. (2005), the radial bias function can be written in terms of the non-linear matter correlation function according to

$$\zeta_0(r, z) = \frac{[1 + 1.17 \xi_{\text{mm}}(r, z)]^{1.49}}{[1 + 0.69 \xi_{\text{mm}}(r, z)]^{2.09}}. \quad (\text{A3})$$

Here the subscript 0 indicates that this empirical fitting function was calibrated using N -body simulations in which the haloes were identified using the friends-of-friends algorithm. We use a slightly modified version of this calibration tuned to reproduce the halo-halo and halo-matter correlation functions for halos identified by the spherical overdensity algorithm (see Paper I). This modification only affects scales smaller than a characteristic scale, r_ψ , such that

$$\zeta(r, z) = \begin{cases} \zeta_0(r, z) & \text{if } r \geq r_\psi \\ \zeta_0(r_\psi, z) & \text{if } r \leq r_\psi \end{cases}. \quad (\text{A4})$$

The characteristic radius, r_ψ , is defined by

$$\log [\zeta_0(r_\psi, z) \xi_{\text{mm}}(r_\psi, z)] = \psi. \quad (\text{A5})$$

Using high resolution numerical simulations for a Λ CDM cosmology, we found in Paper I that $\psi = 0.9$ can accurately describe the halo-halo correlation function on small scales. Since we cannot rule out that the calibration parameter ψ